Developing an atlas of rain-induced leading edge erosion for wind turbine blades in the Dutch North Sea

Marco Caboni[1] and Gerwin van Dalum[2]

[1]TNO, Wind Energy Technology, Westerduinweg 3, 1755 LE Petten, The Netherlands
[2]Whiffle, Molengraaffsingel 8, 2629 JD Delft, The Netherlands

Correspondence: Marco Caboni (marco.caboni@tno.nl)

Abstract. To support the ongoing development of offshore wind energy in The Netherlands and to maintain the current assets, it is essential to provide wind farm operators accurate estimates of wind turbine blade erosion. Unfortunately, there is currently a shortage of information on wind turbine erosion risk, especially in offshore regions. In this work, we developed an atlas detailing rain-induced leading edge erosion for wind turbine blades in the Dutch North Sea, using weather simulations spanning a decade to capture long-term climate patterns. These simulations, based on a meso-scale model, were incorporated into a fatigue-based damage model, linking weather conditions to blades' leading edge erosion. The results reveal that the erosive impact of rainfall on wind turbine blades varies across the Dutch North Sea. The estimated average incubation period, which indicates the leading edge protection system's lifespan, ranges from 8 to 9 years in the southwestern region, decreasing to 6 to 7 years in the northeastern area. This is due to both the higher average wind speeds and greater rainfall amounts occurring in the northeastern locations compared to the southwestern ones. This paper emphasizes that the northeastern regions of the Dutch North Sea, which are being examined for potential wind farm developments post-2030, will encounter higher erosion risks compared to those currently operating in southern locations, possibly requiring enhanced mitigation strategies. Additionally, a year-long comparison of meso-scale simulations, high-resolution large eddy simulations (LES) and measurements revealed that meso-scale simulations estimate 7-20% less damage than LES, which captures more extreme events. Nonetheless, meso-scale simulations and LES reveal alignment in the spatial patterns of erosion-related parameters, confirming that meso-scale simulations produce satisfactory atlases where regional differences are consistently captured with LES. Through the comparison between LES and measurements, it was found that LES estimates 23-66% less damage than actual weather data, due to underestimating larger droplets and recording fewer extreme events.

1 Introduction

The Dutch North Sea is undergoing significant development in wind energy, with numerous wind farms currently operating and more planned (Noordzeeloket, 2024). For developers of offshore wind farms and turbines, assessing the risk of rain-induced leading edge erosion (LEE) is crucial. Raindrops hitting the blades lead to gradual mechanical wear on the surface of their leading edge (Slot et al., 2015). Leading edge wear continues to occur despite the development and implementation of advanced leading edge protection (LEP) systems on modern wind turbine blades (Mishnaevsky et al., 2021). Damaged

blades result in decreased turbine performance (Bak et al., 2020; Maniaci et al., 2020; Vimalakanthan et al., 2023; Castorrini et al., 2023), forcing wind farm operators to conduct frequent, costly, labor-intensive, and possibly hazardous maintenance procedures to fix the blades. LEE poses a significant challenge to the rapid deployment of wind energy, particularly in offshore environments.

LEE is a fatigue-driven process in which each droplet impact contributes to cumulative damage. (Slot, 2021; Mishnaevsky, 2019). The severity of LEE is tied to the frequency and speed of impacts, as well as the drop size distribution (DSD). Although the quantity of impacts and the size of raindrops are linked to rain conditions, the speed of the impacts primarily depends on the turbine's rotational speed, which is linked to wind speed. Thus, evaluating LEE must consider the simultaneous conditions of both rain and wind speed. Caboni et al. (2024) carried out concurrent measurements of rain and wind speed at an offshore platform in the Dutch North Sea, linking the weather conditions to the accumulation of wind turbine damage. Other recent studies focused on evaluating LEE using measurements carried out at onshore and coastal areas (Hasager et al., 2020, 2021; Shankar Verma et al., 2021; Verma et al., 2021; Letson and Pryor, 2023; Hannesdóttir et al., 2024a; Méndez et al., 2024; Pryor et al., 2025b). Numerical techniques can be utilized to bridge the gap in onshore and offshore measurements, providing essential data to assess erosion risks associated with wind energy deployment (Pryor et al., 2023; Hannesdóttir et al., 2024b). Other studies concentrate on creating maps of wind resources without addressing the issue of wind turbine erosion (Nawri et al., 2014; Hahmann et al., 2020; Davis et al., 2023; Larsén et al., 2022; Mortensen et al., 2014; Copernicus-Climate-Change-Service). The report by Pryor et al. (2025a) offer an excellent overview of the various meteorological data sets that have been utilized in the creation of erosion atlases.

The literature review reveals a significant gap in knowledge regarding the large-scale mapping of rain erosion risks for wind turbine blades, particularly in the Dutch North Sea. Hannesdóttir et al. (2024b) incorporated wind turbine erosion into their analysis by creating a rain erosion atlas for the Norwegian and Danish North Sea, along with the Baltic Sea. This was achieved by linking the ERA5 and NORA3 reanalysis datasets to a wind turbine erosion model. Although focusing on the Norwegian and Danish North Sea, the erosion atlas by Hannesdóttir et al. (2024b) covers part of the Dutch North Sea as well, but it is insufficient to determine the differences within the region. This is because it does not encompass a significant portion of the Dutch North Sea, particularly the central and southern areas where most current Dutch wind farms are situated. This study aims to fill this gap by creating an atlas based on long-term meso-scale simulations to assess the risk of LEE in the Dutch North Sea. By spanning 10 years to capture the long-term precipitation climate, this study surpasses the erosion atlas by Hannesdóttir et al. (2024b), which was developed over 5 years. Additionally, it offers slightly better spatial resolution (2 km instead of 3 km) while maintaining the same temporal resolution (1 hour).

As part of this project, we aimed to identify potential improvements for simulations used to determine erosion atlases. To achieve this goal, we compared our meso-scale simulations with a high-resolution large eddy simulation (LES) setup over the course of a year over the Dutch North Sea. The advantage of using LES over meso-scale simulations is that it involves less spatial and temporal averaging of local variables, allowing it to better capture extreme precipitation events. LES simulations indeed were carried out with a spatial resolution of 120 meters and a temporal resolution of one minute. The drawback of LEE is that it requires significantly more computational resources than mesoscale simulations. To date, no such simulation

and comparison has been published. To gain a deeper understanding of the simulations, LES were also compared with the experimental data published by Caboni et al. (2024), introducing an additional novel aspect.

The remainder of this paper is organized into three sections. The methodology section details the models and simulations, including the methodology used to evaluate erosion damage and the measurements utilized to provide a comparison to the simulations. In the results section, we present the developed atlas, along with a comparison between measurements and simulations. The final section will draw conclusions and outline future research directions.

2 Methods

2.1 Whiffle's ASPIRE weather simulations

The innovative numerical method used in this research relies on Whiffle's LES model ASPIRE (Atmospheric Simulation Platform for Innovation, Research, and Education). ASPIRE started as a GPU implementation of the DALES (Dutch Atmospheric Large-Eddy Simulation) model (Heus et al., 2010; Schalkwijk et al., 2012) that has since received numerous improvements that allow it to be used as an operational weather model. Its main innovation is that the model's calculations are highly parallelized using the capabilities of the GPU, which cuts down the runtime by several orders of magnitude compared to traditional implementations on the CPU. Crucially, this allows for simulations on a much larger domain and/or a much higher resolution at the same computational cost. ASPIRE can also run meso-scale simulations that do not resolve any turbulence like in LES, but benefit from the same computational speed-up.

ASPIRE was used to create a precipitation atlas for the Dutch North Sea by simulating weather conditions over a long period of time. A description of the model, its governing equations, and its boundary conditions can be found in Baas et al. (2023). Following the methods described by Storey and Rauffus (2024), simulations of historical weather conditions are performed by coupling large-scale data from ECMWF's ERA5 reanalysis dataset (Hersbach et al., 2020) to the lateral boundaries of a meso-scale version of the model. In a similar manner, this meso-scale simulation is in turn coupled to the boundaries of a nested high resolution LES. Both the meso-scale simulation and the LES use an implementation of the microphysics model by Grabowski (1998), which locally calculates the rate of rain droplet formation and simulates the subsequent precipitation. Since ASPIRE works with model time steps of a few seconds, it is able to capture short-lived events such as the high rain rate events that are of special interest for this study.

Within ASPIRE, moisture is treated using two prognostic variables, distinguishing between the total non-precipitating specific humidity q_t consisting of water vapor and non-precipitating liquid and ice water, and precipitating water q_r. The former is diagnostically partitioned into its components using an all-or-nothing scheme that assumes the water to be homogeneously distributed over a grid cell. As such, grid cells with q_t below the local saturation mixing ratio q_{sat} contain no clouds, whereas any q_t above saturation is immediately interpreted as non-precipitating liquid or ice water, depending on the temperature. Following Grabowski (1998), this cloud water content is subsequently used to calculate autoconversion and accretion rates for droplet formation, as well as deposition and evaporation rates. Finally, precipitation of the formed droplets is accounted for by an additional advective term that makes the droplets fall. The resulting change in precipitating water content q_r is subtracted

from q_t, such that the total amount of water is conserved. Note that although ASPIRE works with a single prognostic precipitation variable q_r, different species (most importantly rain and snow) are diagnosed using a temperature-based partitioning, each with their own version of the DSD, mass-diameter relation, and fall velocity. However, as this study is specifically about rain-induced LEE, the remainder of this section focuses solely on rain.

To determine the incubation period, information about the rain DSD is required. This information can be extracted from the simulations by utilizing the fact that the underlying microphysics model assumes the Marshall-Palmer distribution (Marshall and Palmer, 1948):

$$N(D) = N_0 \exp(-\lambda D), \tag{1}$$

where $N(D)$ is the DSD in m^{-4} as a function of drop diameter D, λ is a shape parameter, and N_0 is a fixed prefactor. The shape parameter λ depends on the local amount of rain water q_r (in kg kg^{-1}), the local air density ρ, and the density of water ρ_w through the following relation:

$$\overline{\rho q_r} = \int_0^\infty \mathrm{d}D \frac{\pi}{6} D^3 \rho_w \cdot N(D) = \pi \rho_w N_0 \lambda^{-4}. \tag{2}$$

Combined with the fall velocity used in ASPIRE (Lin et al., 1983),

$$v_t(D) = a D^b \left(\frac{\rho_0}{\rho}\right)^{1/2}, \tag{3}$$

where a, b and ρ_0 are empirical constants, the rain rate RR can be calculated as a function of the shape parameter λ by using its definition:

$$\overline{\text{RR}} = \int_0^\infty \mathrm{d}D \frac{\pi}{6} D^3 \cdot N(D) \cdot v_t(D) = \frac{\pi}{6} N_0 a \left(\frac{\rho_0}{\rho}\right)^{1/2} \lambda^{-(4+b)} \Gamma(4+b), \tag{4}$$

with $\Gamma(x)$ being the gamma function. As a best estimate for the DSD from the simulation, we assume the rain rate to be constant over the output interval, and use its value to determine the shape parameter (and by extension the corresponding DSD) by inverting Equation 4. The reason we do this is because rain-related quantities such as λ and the rain rate can vary strongly on short time scales, while simulation output is always an average over a certain period of time and not an instantaneous value. This method of dealing with the consequences of temporal averaging guarantees that the estimated DSD matches the total precipitation during a given time interval, which is not the case with most other methods due to the nonlinearity of the equations involved. Since the rain rate fluctuates constantly, the accuracy of this estimated DSD increases with decreasing output intervals.

Within the framework of this research, two ASPIRE simulations have been performed. The first is a high resolution 1-year LES (March 2022 - March 2023) covering most of the Dutch North Sea. In addition, a larger but much lower resolution stand-alone meso-scale simulation was done, covering a period of 10 years (2014 – 2023) with a domain size of over 1,000 kilometers. The goal of the latter is to provide data for an atlas that spans a long period of time, while the former is a shorter

Table 1. Summary of the settings used in the simulations. Note that the vertical levels are non-uniformly distributed.

	High resolution 1-year LES	Stand-alone 10-year meso-scale simulation
Period	21/03/2022 - 20/03/2023	01/01/2014 - 31/12/2023
Dimensions	245.76 km x 384 km x 8 km	1,024 km x 1,024 km x 8 km
Horizontal resolution	120 m x 120 m	2 km x 2 km
Number of vertical levels	64	128
Output sampling method	1-minute averages	hourly averages

but much higher fidelity simulation that can be used to verify the latter. The settings used for the simulations are summarized in Table 1.

All simulations were performed "in series" on a per-month basis, i.e. the next simulation starting from the end state of the previous simulation, so only the first day of a month required spin-up time. Furthermore, the output, consisting of two-dimensional grids of time series for multiple variables, most importantly includes rain rate and wind speed. The output is always sampled at 100 m elevation, and it is sampled locally (no spatial averaging over multiple grid points).

2.2 Accumulated damage estimation

The erosion process is influenced by the fatigue properties of the blade's LEP systems, as well as the size and number of droplets impacting the surface at a specific speed. Wear particle emission from the leading edge begins once the incubation period ends. Typically, the incubation period is considered the LEP system's lifespan (Slot, 2021). In this study, we estimated the incubation period using the "ASTM - Multiple linear regression fit equations," which include a modified dependence on drop size (Slot et al., 2025). This model applies only to liquid drop impacts. Heymann (1979) developed multiple linear regression fit equations for the incubation life based on an extensive ASTM test program, where each material is characterized by its normalized incubation resistance number (NOR). To determine the NOR for current LEP systems on wind turbine blades, we conducted a literature review on rotating arm rain erosion tests on LEP systems (Caboni et al., 2025). The NOR values for current LEP systems range from 0.001 to 0.033. For details on the equations used, the reader is referred to Caboni et al. (2024). To consider the cumulative impact of varying rain and wind speed conditions on the erosion process, assuming linear damage accumulation, the Palmgren-Miner's rule was applied. The accumulated damage is represented by a parameter F, which starts at zero at the onset of the erosion process and reaches one at the conclusion of the incubation period.

For simplicity, this study concentrated on the accumulated damage at the blade tips of the virtual IEA 15 MW reference wind turbine (Gaertner et al., 2020), which have a maximum tip speed of 95 m/s and utilize a polyurethane LEP system with an estimated NOR of 0.003. The cumulative damage is closely linked to the relative impact velocity between the blade and the raindrops. This velocity is influenced by the blade's rotational speed, the fall velocity of the droplets, and the aerodynamic interactions between the rain and the wind (Barfknecht and von Terzi, 2023). For simplicity in this work, we assumed that

Figure 1. Map illustrating the locations in The Netherlands where simultaneous wind and rain measurements were conducted as part of the PROWESS project (Caboni et al., 2024). Image courtesy of © Google Earth.

the fall velocity of the raindrops is negligible compared to the blade tip speed and that there are no aerodynamic interactions between the droplets and the wind. Therefore, we considered the impact speed between the blade and the raindrops to be equal to the tangential tip speed. The tangential tip speed is determined by the rotor speed, which is connected to the wind speed. The current maximum tip speed of modern offshore wind turbines is around 90 m s^{-1} (Wind Energy - The Facts, 2024).

2.3 Rain and wind speed measurements

From March 2022 to March 2023, TNO conducted simultaneous measurements of rainfall and wind speed at three locations in The Netherlands (Caboni et al., 2024). These sites included an offshore location (LEG), a coastal location (GEHALX), and an onshore location (EWTW), as shown in Figure 1. Rainfall was measured using OTT Parsivel^2 disdrometers at LEG and GEHALX, and a Thies LPM disdrometer at EWTW. Wind speed was recorded with cup anemometers at EWTW and GEHALX, and a Leosphere WindCube V2 LiDAR at LEG. To focus on rain-induced erosion, events involving snow and hail were excluded, leaving only rainy periods. Rainfall data was collected at a frequency of 1 Hz, while wind speed data was recorded at 0.1 Hz.

For each observation interval, we calculated the rain parameters like intensity and amount by using the measured DSD and droplet fall velocity using the formulas presented by Tilg et al. (2020). However, it is essential to note that DSD measurements obtained from current sensors, such as disdrometers, remain quite uncertain (Letson and Pryor, 2023; Caboni et al., 2024; Hannesdóttir et al., 2024a). This is due to the fact that these sensors and their algorithms are typically optimized to accurately detect total precipitation amounts rather than the DSD itself. Disdrometers indeed detect droplets, and the rain amount is derived from the DSD. However, disdrometers cannot measure the full spectrum of droplet sizes and therefore rely on algorithms

6

that make assumptions to improve the estimation of the rain amount. In our experience this seems to be rather site/precipitation dependent. Additionally, uncertainties in sensor calibration and potential measurement errors caused by wind turbulence, insects, or, at offshore locations, sea spray contribute to the overall uncertainty in disdrometer measurements.

3   Results

In this section we present the LEE atlas and show the comparison between measurements and ASPIRE simulations. The atlas was developed by using a stand-alone 10-year meso-scale simulation. The comparison between measurements and ASPIRE simulations was carried out over the span of a year, during which stand-alone meso-scale simulations, high-resolution LES, and measurements were available. Initially, meso-scale simulations were compared to LES, followed by a comparison of LES to measurements.

3.1   Dutch North Sea wind turbine blades' rain-induced leading edge erosion atlas

Meso-scale simulations are conducted to develop the long-term atlas. Figures 2, 3 4 and 5 illustrate contour maps of the annual mean wind speed at 100 meters above the ground and mean sea level, annual rainfall, annual accumulated damage, and annual incubation period, respectively. The contour maps presented here are derived by averaging the yearly simulation results over a 10-year period, from 2014 to 2023. Coastlines are depicted by solid black lines on the maps, while dashed lines indicate the boundaries of the Dutch North Sea. Current, planned, and (estimated) future wind farm areas (North-Sea-Energy, 2024) are represented by blue, red, and green lines, respectively.

Figure 3 shows that the incubation period within the Dutch North Sea varies. It ranges from 8 to 9 years in the southwest and decreases to 6 to 7 years as one moves towards the northeast. The variation in the incubation period is linked to differences in mean wind speed and annual rainfall. As shown in Figure 4, the wind speed is approximately 9.6 m/s in the south and increases to about 10.6 m/s in the northeast. Additionally, the northeast experiences higher rainfall, up to 600 mm annually, compared to 500 mm in the south, as shown in Figure 5.

Therefore, in the northeastern part of the Dutch North Sea, which is a potential area for future wind farms, developers will need to consider the greater impact of LEE compared to wind farms in the southern regions. The reason for this is that these areas experience higher wind speeds and greater rainfall. To clarify the differences between the southern and northern areas, Figure 6 presents a comparison of the simulated annual rainfall and accumulated damage at two locations: one at the LEG offshore platform (situated in the southwest) and the other in the northeast, located at coordinates 53.9968, 6.0106. It appears that in the southwest there was more rainfall with relatively higher intensity, whereas in the northeast, more rain fell but with relatively lower intensity. However, in the northeast, more rain falls at higher wind speeds, which contributes to greater erosivity in that region.
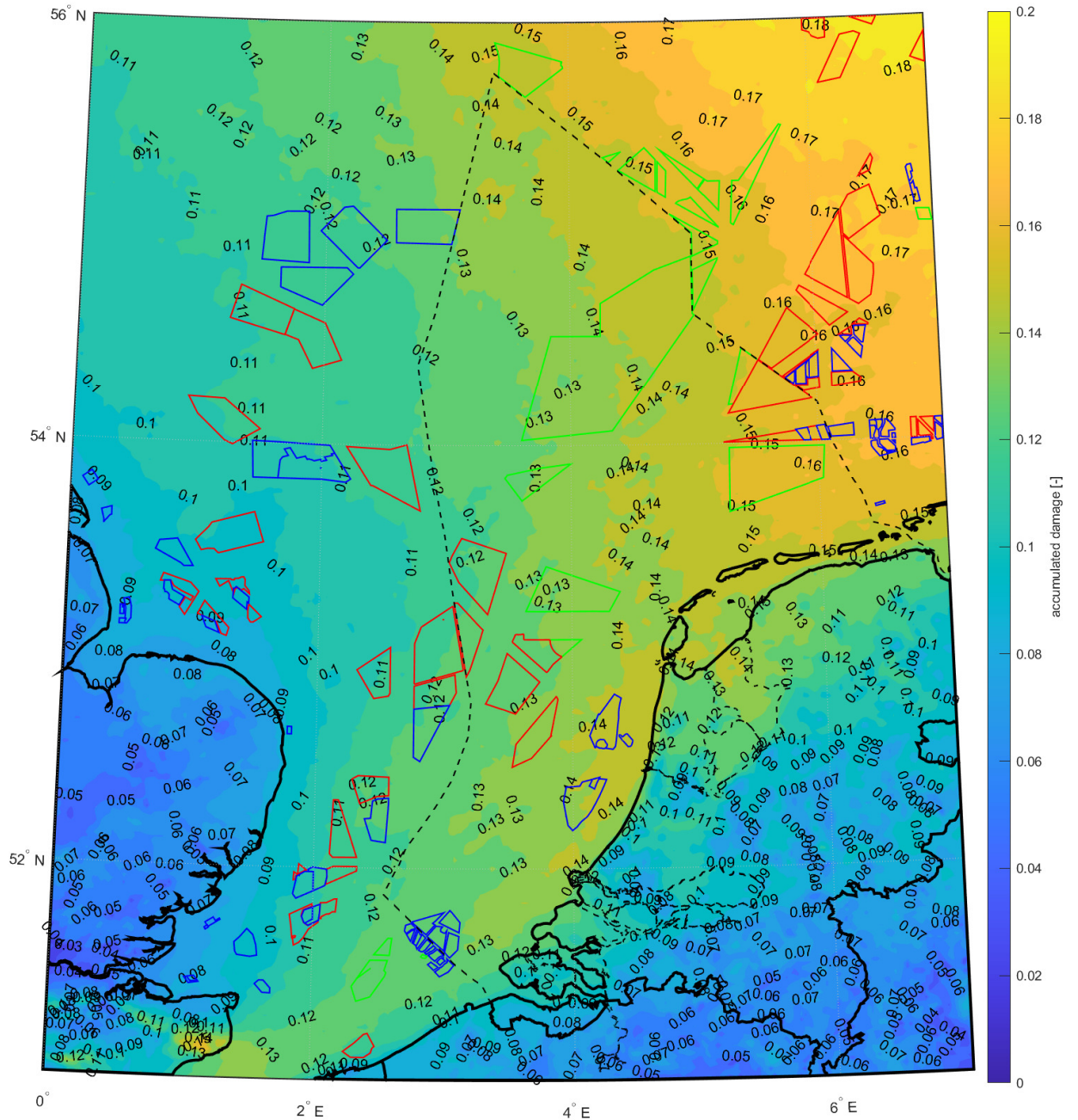
Figure 2. Contour map of yearly accumulated damage based on 10 years of meso-scale simulations. Zones of currently operational wind farms are depicted in blue, while areas of wind farms planned to be operational before 2030 and search areas for wind farms to be commissioned after 2030 are depicted in red and green, respectively. Dashed lines depict the boundaries of the Dutch North Sea.
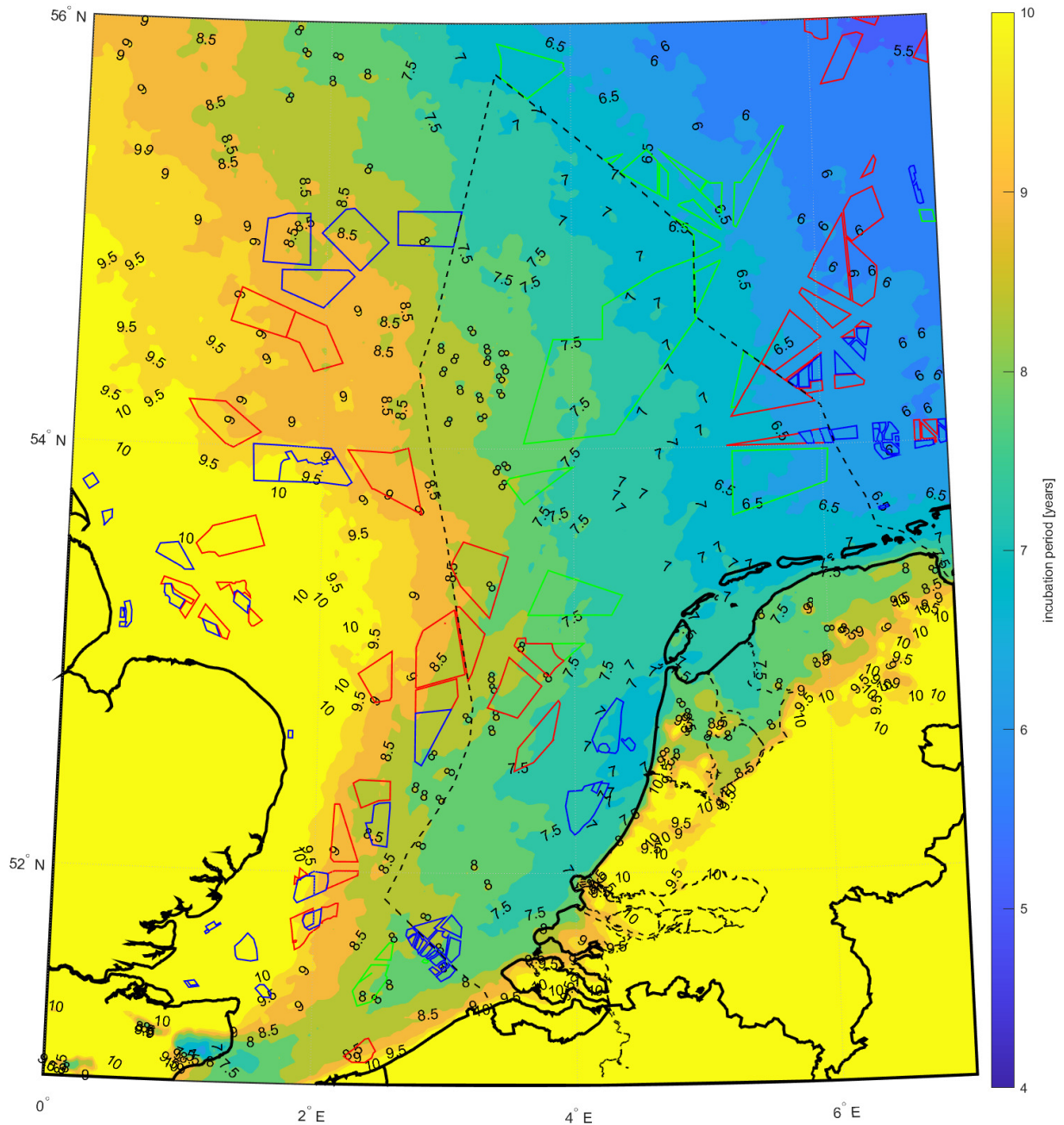
Figure 3. Contour map of yearly incubation period based on 10 years of meso-scale simulations. Zones of currently operational wind farms are depicted in blue, while areas of wind farms planned to be operational before 2030 and search areas for wind farms to be commissioned after 2030 are depicted in red and green, respectively. Dashed lines depict the boundaries of the Dutch North Sea. The color scale of this map is adapted to highlight differences across the Dutch North Sea. This resulted in nearly constant coloring in other areas, which should not be interpreted as constant values, but rather as values outside the selected scale.
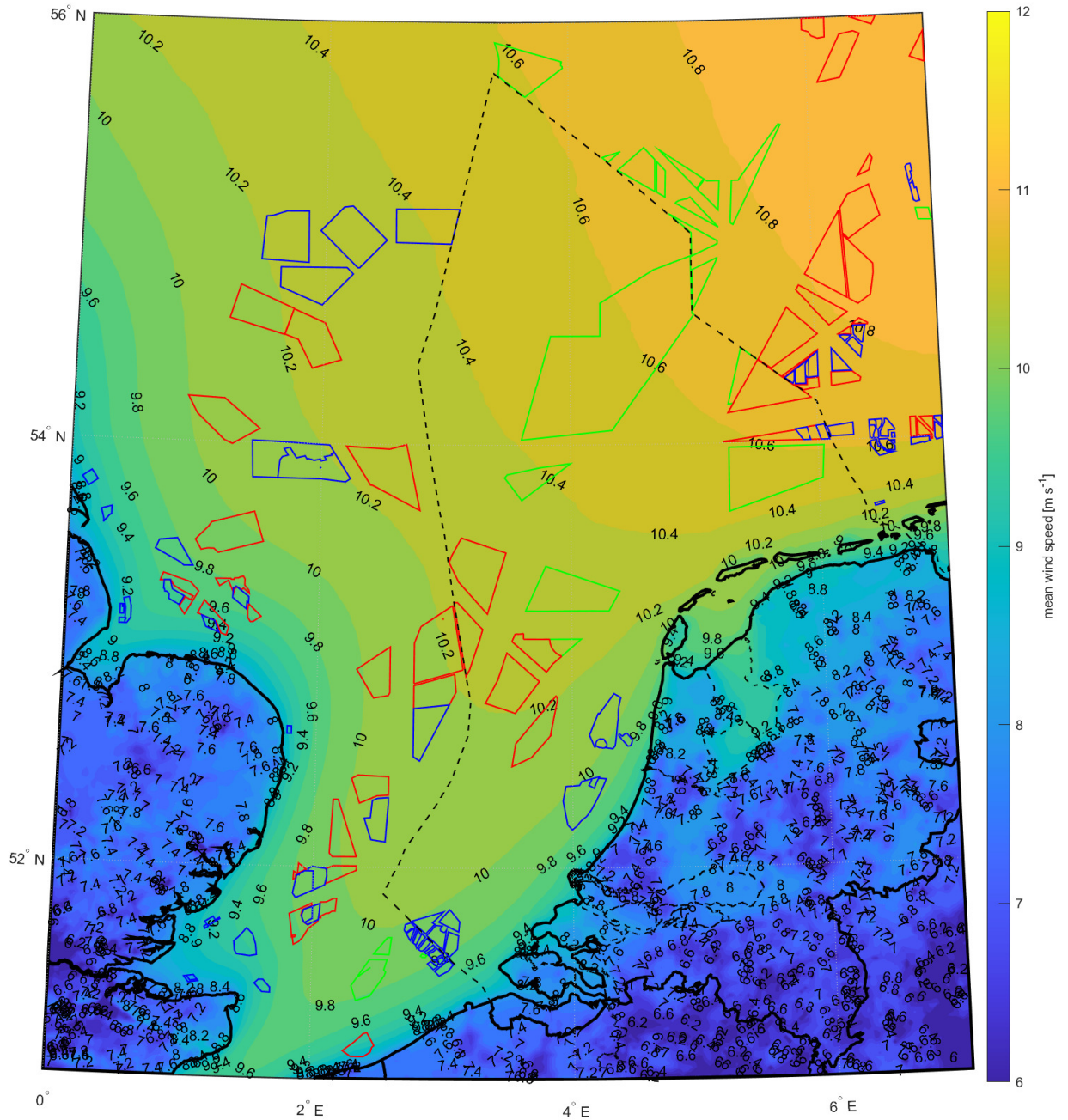
Figure 4. Contour map of yearly mean wind speed at 100 m above the ground and mean sea level based on 10 years of meso-scale simulations. Zones of currently operational wind farms are depicted in blue, while areas of wind farms planned to be operational before 2030 and search areas for wind farms to be commissioned after 2030 are depicted in red and green, respectively. Dashed lines depict the boundaries of the Dutch North Sea.
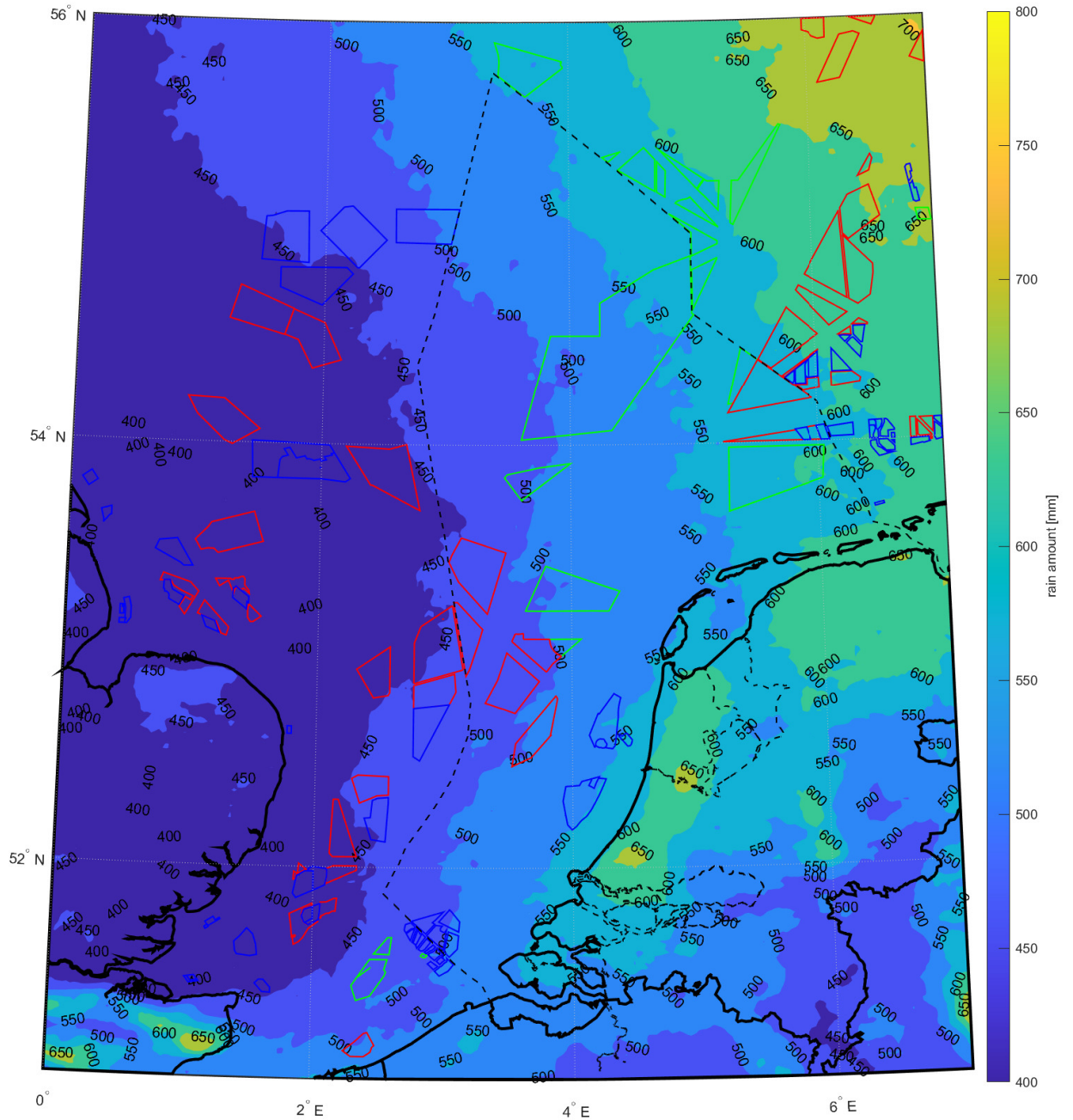
Figure 5. Contour map of yearly rain amount based on 10 years of meso-scale simulations. Zones of currently operational wind farms are depicted in blue, while areas of wind farms planned to be operational before 2030 and search areas for wind farms to be commissioned after 2030 are depicted in red and green, respectively. Dashed lines depict the boundaries of the Dutch North Sea.

RA [mm], ASPIRE (meso-scale) LEG 2014-2023 (n = 21269)

WS [m s^{-1}] \ RR [mm h^{-1}]	0.5	3	7.5	15	>20	Σ
2.5	144.3	213.2	83.19	33.49	0	474.2
7.5	532.9	735.5	172.2	77.51	0	1518
12.5	749.6	848.6	169.8	57.68	0	1826
17.5	485.1	650.3	60.86	0	0	1196
22.5	141.7	190	5.771	0	0	337.5
27.5	14.19	25.05	5.762	10.46	0	55.46
>30	2.256	17.86	0	13.33	0	33.45
Σ	2070	2681	497.6	192.5	0	5441

RA [mm], ASPIRE (meso-scale) 53.9968-6.0106 2014-2023 (n = 30364)

WS [m s^{-1}] \ RR [mm h^{-1}]	0.5	3	7.5	15	>20	Σ
2.5	158.6	135.6	50.63	10.21	0	355.1
7.5	609.5	610.3	96.77	23.91	27.11	1368
12.5	1033	916.6	134.3	10.4	0	2094
17.5	701.1	750.7	68.3	0	0	1520
22.5	222.9	255	10.46	10.52	0	498.9
27.5	24.54	51.05	28.54	0	0	104.1
>30	0.6348	11.22	0	0	0	11.86
Σ	2750	2730	389	55.04	27.11	5952

F [-], ASPIRE (meso-scale) LEG 2014-2023 (n = 21269)

WS [m s^{-1}] \ RR [mm h^{-1}]	0.5	3	7.5	15	>20	Σ
2.5	0.001993	0.003145	0.001912	0.0007593	0	0.00781
7.5	0.03725	0.06305	0.01627	0.00886	0	0.1254
12.5	0.227	0.3307	0.07889	0.02898	0	0.6656
17.5	0.1504	0.2574	0.02867	0	0	0.4365
22.5	0.04434	0.07577	0.002662	0	0	0.1228
27.5	0	0	0	0	0	0
>30	0	0	0	0	0	0
Σ	0.461	0.7301	0.1284	0.0386	0	1.358

F [-], ASPIRE (meso-scale) 53.9968-6.0106 2014-2023 (n = 30364)

WS [m s^{-1}] \ RR [mm h^{-1}]	0.5	3	7.5	15	>20	Σ
2.5	0.00214	0.002238	0.001609	0.0003474	0	0.006334
7.5	0.04432	0.05824	0.008836	0.003357	0.007791	0.1225
12.5	0.3069	0.3567	0.06113	0.005161	0	0.7299
17.5	0.2159	0.2948	0.03233	0	0	0.5431
22.5	0.06894	0.0997	0.004756	0.005312	0	0.1787
27.5	0	0	0	0	0	0
>30	0	0	0	0	0	0
Σ	0.6382	0.8118	0.1087	0.01418	0.007791	1.581

Figure 6. Yearly rain amount and accumulated damage sorted out into wind speed and rain rate bins. This figure compares a location situated in the southern part of the Dutch North Sea (LEG platform) with a location in the northeast (with coordinates 53.9968, 6.0106). The ASPIRE results presented in this figure are obtained from the meso-scale simulations.

3.2   Comparison between measurements and ASPIRE

The comparison between measurements and ASPIRE simulations is presented in three sections. The first section deals with the comparison of aggregated figures related to erosion, such as rain amount and accumulated damage, obtained using measurements, LES, and meso-scale simulations. The second section focuses on a more detailed comparison between meso-scale and high resolution LES. The third section focuses on comparing measurements with high-resolution LES, including DSD and droplet fall velocities.

3.2.1   Comparison of aggregate erosion figures between measurements, high resolution LES, and stand-alone meso-scale simulation

In this section, numerical results and measurements over one year are compared at the three aforementioned locations, estimating aggregate erosion figures such as yearly rainfall and accumulated damage. Numerical data and measurements are utilized to assess the accumulated tip damage of the IEA 15 MW reference wind turbine, virtually installed at the specified locations. It is assumed that the turbine blades utilize a polyurethane LEP system. Table 2 presents a comparison of aggregated meteorological and erosion data between simulations and experiments at the three locations.

LES overestimate the average wind speed during rainy events at LEG and EWTW by up to 6%, while at GEHALX, it is underestimated by 8%. The predicted rain amount is up to 13% lower than the measurements at LEG and EWTW, while at GEHALX, it is 13% higher. To provide further insight into the wind speed comparison, Figure 7 displays the measured and LES and meso-scale simulated probability distribution functions for wind speed during rainy events. By utilizing the measured annual wind speed and rainfall, we calculated the yearly accumulated damage. Taking the reciprocal of this accumulated damage provides an estimate of the incubation period (in years). As seen in Table 2, LES underestimate the accumulated damage by 23% at EWTW, 45% at GEHALX, and 66% at LEG.

Compared to measurements, the meso-scale average wind speed during rain is underestimated by 2% at LEG and 10% at GEHALX, while it is overestimated by about 4% at EWTW. The meso-scale rain amount is underestimated by 4% at LEG and 8% at EWTW, but overestimated by approximately 21% at GEHALX. Consequently, meso-scale simulations underestimate accumulated damage by 29% at EWTW, 55% at GEHALX, and 70% at LEG.

In terms of absolute values, the accumulated damage is significantly lower when either meso-scale or LES simulations are used compared to measurements. The accumulated damage predicted with LES aligns more closely with experimental results than when meso-scale simulations are employed. As demonstrated in the following paragraph, this is because our LES setup is more effective at capturing extreme events than our meso-scale simulation, especially those characterized by high intensity and large wind speeds. In terms of trends, the comparison between measurements and simulations reveals differences as well. According to the measurements, the accumulated damage at EWTW is 58% less and at GEHALX is 42% less compared to LEG. According to LES, the accumulated damage at EWTW and GEHALX is 7% less compared to LEG. According to the meso-scale simulations, the accumulated damage is 7% more at EWTW while it is 7% less at GEHALX compared to LEG.

Table 2. Comparison between measured and simulated average wind speed during rainy intervals, total rainfall, accumulated damage, and estimated incubation period, based on one year of measurements from March 21, 2022, to March 21, 2023. The figure shows ASPIRE's numerical results from the high resolution LES and stand-alone meso-scale simulation.

location	source	WS [m s^1]	RA [mm]	F [-]	IP (= F^{-1}) [yr]
LEG	meas.	11.21	555	0.43	2.34
	ASPIRE (LES)	11.60 (3.49 %)	499 (-10.07 %)	0.15 (-65.77 %)	6.84 (192.11 %)
	ASPIRE (meso-scale)	10.99 (-1.93 %)	530 (-4.42 %)	0.12 (-70.75 %)	8.00 (241.90 %)
EWTW	meas.	8.56	591	0.18	5.54
	ASPIRE (LES)	9.08 (6.01 %)	512 (-13.44 %)	0.14 (-23.33 %)	7.23 (30.43 %)
	ASPIRE (meso-scale)	8.87 (3.63 %)	542 (-8.42 %)	0.13 (-29.12 %)	7.82 (41.09 %)
GEHALX	meas.	10.82	457	0.25	3.93
	ASPIRE (LES)	9.96 (-7.98 %)	520 (13.83 %)	0.14 (-44.56 %)	7.09 (80.38 %)
	ASPIRE (meso-scale)	9.72 (-10.14 %)	555 (21.44 %)	0.11 (-55.20 %)	8.77 (123.20 %)
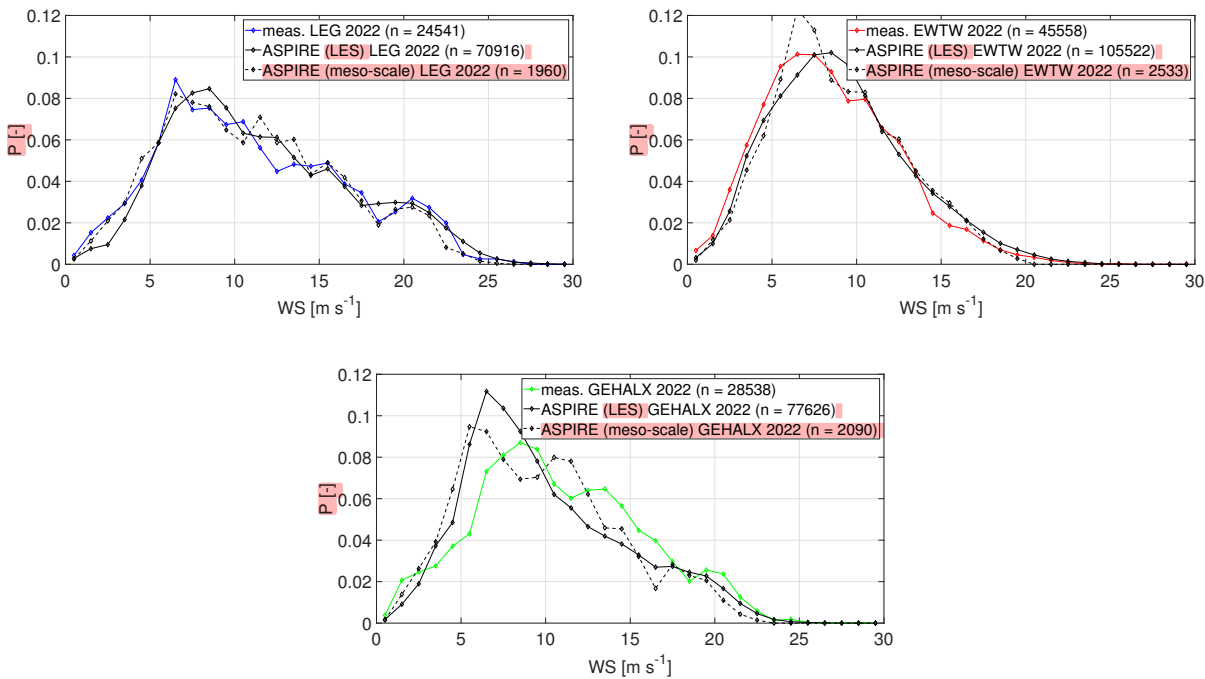
Figure 7. Comparison of measured and simulated probabilities of wind speed during rainy intervals at the measurement sites. Here, the numerical results are from the high resolution LES.

14

3.2.2 Detailed comparison between meso-scale simulations and high resolution LES

Table 2 shows that the estimated accumulated damage is higher when using LES compared to meso-scale simulations for all the studied locations. Specifically, it is 20%, 7%, and 21% higher at LEG, EWTW, and GEHALX, respectively. The explanation for this can be found in the distribution of simulated rainfall across different rain rates and wind speed conditions. Figure 8, which depicts the annual rainfall broken down into wind speed and rain rate bins. According to this figure, LES predicts less total rain amount at all locations compared to meso-scale simulations. However, the distribution of rainfall varies across wind speed and rain rate bins. More specifically, LES captures more extreme events, with higher rainfall occurring at greater rain rates and higher wind speeds. As depicted in Figure 9, these extreme events result in larger accumulated damage because high-intensity rain events contain larger and more erosive raindrops. As mentioned, the ability of our LES setup to capture more extreme events than meso-scale simulations is related to temporal averaging. Meso-scale simulations use a one-hour temporal resolution, while LES use a one-minute temporal resolution. Temporal averaging implies that the rain rate remains constant over the output interval. The rain rate varies significantly within an hour, with extreme events occurring over minutes. This is why the temporal resolution used by LES allows them to capture these events, while they are averaged out by the meso-scale simulations.

Figures 10,11,12, and 13 depict the comparison between meso-scale simulations and high-resolution LES on the derived contour maps for the annual mean wind speed at 100 meters above ground and mean sea level, annual rainfall, annual accumulated damage, and annual incubation period, respectively. It is observed that these calculations yield consistent maps. The side-by-side comparison of the contour maps obtained using meso-scale simulations and LES reveals alignment in the spatial patterns, confirming that meso-scale simulations produce satisfactory results where regional differences are captured consistently with LES.

In summary, Figures 10,11,12, and 13 provide a convincing argument supporting the claim that meso-scale simulations can produce satisfactory atlases. However, Figure 8 and Figure 9 effectively illustrate the extent to which LES is superior in capturing more extreme events. LES is much better at capturing local short-lived extreme events, which are of high importance for LEE, but it requires significantly more computational resources.

3.2.3 Detailed comparison between measurements and high resolution LES

To explore the aforementioned differences between simulations and measurments in total accumulated damage in greater detail, we present the annual rainfall, total damage and accumulated damage per rain amount organized into bins based on wind speed and rain rate in Figures 14, 15 and 16, respectively. The findings in this section remain consistent whether we consider LES or meso-scale simulations. The primary difference, as previously explained, is that LES captures more extreme events compared to meso-scale simulations. Both LES and meso-scale simulations rely on the same model for the DSD. Therefore, for the sake of brevity, we will conduct this analysis using only the LES.

Damage accumulation is more significant during extreme events, namely high rain intensity and strong wind speeds. Caboni et al. (2024) noted that at LEG 30% of the yearly damage is accumulated over just 12 hours, in which the wind speed is greater

RA [mm], ASPIRE (meso-scale) LEG 2022 (n = 1960)

WS [m s⁻¹]	0.5	3	7.5	15	>20	Σ
2.5	16.65	25.75	9.064	0	0	51.47
7.5	54.58	88.52	22.99	0	0	166.1
12.5	66.91	67.17	22.94	0	0	157
17.5	48.35	56.72	0	0	0	105.1
22.5	18.82	31.74	0	0	0	50.56
27.5	0.004318	0	0	0	0	0.004318
>30	0	0	0	0	0	0
Σ	205.3	269.9	55	0	0	530.2

RR [mm h⁻¹]

RA [mm], ASPIRE (LES) LEG 2022 (n = 70916)

WS [m s⁻¹]	0.5	3	7.5	15	>20	Σ
2.5	4.299	14.94	8.75	4.798	0.3496	33.14
7.5	27.58	72.55	20.48	11.92	0.7256	133.3
12.5	39.62	60.82	26.5	12.12	3.545	142.6
17.5	32.94	54.52	21.8	9.905	1.264	120.4
22.5	15.85	41.23	8.602	0.7403	0	66.43
27.5	1.191	1.637	0.1586	0	0	2.987
>30	0.004303	0	0	0	0	0.004303
Σ	121.5	245.7	86.29	39.49	5.884	498.8

RR [mm h⁻¹]

RA [mm], ASPIRE (meso-scale) EWTW 2022 (n = 2533)

WS [m s⁻¹]	0.5	3	7.5	15	>20	Σ
2.5	24.82	25.72	0	0	0	50.54
7.5	89.82	89.57	6.153	0	0	185.5
12.5	101.2	114.7	27.33	0	0	243.2
17.5	31.96	24.8	5.512	0	0	62.28
22.5	0	0	0	0	0	0
27.5	0	0	0	0	0	0
>30	0	0	0	0	0	0
Σ	247.8	254.8	39	0	0	541.6

RR [mm h⁻¹]

RA [mm], ASPIRE (LES) EWTW 2022 (n = 105522)

WS [m s⁻¹]	0.5	3	7.5	15	>20	Σ
2.5	10.58	20.45	2.968	1.096	1.167	36.25
7.5	44.98	84.79	21.22	4.75	2.425	158.2
12.5	59.73	115.7	34.71	13.76	0.3519	224.2
17.5	22.59	47.63	9.686	3.707	0.3377	83.95
22.5	3.061	5.978	0.1849	0	0	9.224
27.5	0.04337	0.04576	0	0	0	0.08913
>30	0	0	0	0	0	0
Σ	141	274.6	68.78	23.31	4.282	511.9

RR [mm h⁻¹]

RA [mm], ASPIRE (meso-scale) GEHALX 2022 (n = 2090)

WS [m s⁻¹]	0.5	3	7.5	15	>20	Σ
2.5	18.99	49.75	0	11.26	0	80
7.5	72.75	110.2	17.67	0	0	200.7
12.5	76.88	75.98	13.28	0	0	166.1
17.5	33.71	58.51	5.585	0	0	97.8
22.5	8.428	1.715	0	0	0	10.14
27.5	0	0	0	0	0	0
>30	0	0	0	0	0	0
Σ	210.8	296.2	36.53	11.26	0	554.7

RR [mm h⁻¹]

RA [mm], ASPIRE (LES) GEHALX 2022 (n = 77626)

WS [m s⁻¹]	0.5	3	7.5	15	>20	Σ
2.5	8.08	14.03	5.031	7.744	0.3482	35.23
7.5	41.92	87.25	28.02	17.83	3.075	178.1
12.5	40.55	65.98	26.77	19.55	4.285	157.1
17.5	25.67	55.95	17.46	12.93	5.554	117.6
22.5	8.257	17.25	1.857	1.871	2.205	31.43
27.5	0.1416	0.3932	0	0	0	0.5348
>30	0	0	0	0	0	0
Σ	124.6	240.8	79.13	59.94	15.47	520

RR [mm h⁻¹]

Figure 8. Annual rainfall categorized into bins based on wind speed and rain rate. Presented here are the numerical results from meso-scale simulations and high resolution LES.

than 17.5 m s⁻¹ and the rain rate is greater than 7.5 mm h⁻¹. In fact, high-intensity events feature a greater number of relatively large droplets compared to low-intensity events. Larger droplets are more erosive than smaller ones when comparing the same volume of liquid (Barfknecht and von Terzi, 2024; Slot et al., 2025). As noted earlier, wind speed also influences LEE. At higher wind speeds, the blades rotate faster, resulting in a greater impact speed between the rain droplets and the blades. Figures 14 and 15 show that the extreme events differ between measurements and simulations, offering a first explanation for the variations in accumulated damage. Except for GEHALX, both LEG and EWTW have recorded more extreme events than those predicted by simulations. The difference in extreme events is especially pronounced at LEG, resulting in significant variation in accumulated damage. Currently, the authors cannot explain why extreme events are more underestimated at LEG compared

F [-], ASPIRE (meso-scale) LEG 2022 (n = 1960)

WS [m s⁻¹]	0.5	3	7.5	15	>20	Σ
2.5	0.0002718	0.0002193	0.0003026	0	0	0.0007937
7.5	0.003592	0.00633	0.000729	0	0	0.01065
12.5	0.02023	0.02667	0.01057	0	0	0.05747
17.5	0.01508	0.02251	0	0	0	0.03759
22.5	0.005866	0.01259	0	0	0	0.01846
27.5	0	0	0	0	0	0
>30	0	0	0	0	0	0
Σ	0.04505	0.06832	0.0116	0	0	0.125

RR [mm h⁻¹]

F [-], ASPIRE (LES) LEG 2022 (n = 70916)

WS [m s⁻¹]	0.5	3	7.5	15	>20	Σ
2.5	6.075e-05	0.0002241	0.0001497	0.0001397	1.323e-05	0.0005875
7.5	0.00201	0.007933	0.003113	0.001941	3.817e-05	0.01503
12.5	0.01219	0.0236	0.0123	0.00619	0.002038	0.05632
17.5	0.01052	0.02179	0.01031	0.005147	0.0007278	0.0485
22.5	0.005048	0.01636	0.004047	0.0003769	0	0.02583
27.5	0	0	0	0	0	0
>30	0	0	0	0	0	0
Σ	0.02983	0.0699	0.02992	0.0138	0.002818	0.1463

RR [mm h⁻¹]

F [-], ASPIRE (meso-scale) EWTW 2022 (n = 2533)

WS [m s⁻¹]	0.5	3	7.5	15	>20	Σ
2.5	0.0003739	0.0005827	0	0	0	0.0009566
7.5	0.006443	0.0106	0.0004858	0	0	0.01753
12.5	0.03057	0.04437	0.01251	0	0	0.08745
17.5	0.009888	0.009506	0.002525	0	0	0.02192
22.5	0	0	0	0	0	0
27.5	0	0	0	0	0	0
>30	0	0	0	0	0	0
Σ	0.04727	0.06506	0.01552	0	0	0.1279

RR [mm h⁻¹]

F [-], ASPIRE (LES) EWTW 2022 (n = 105522)

WS [m s⁻¹]	0.5	3	7.5	15	>20	Σ
2.5	0.000151	0.0003677	8.788e-05	1.253e-05	0	0.0006191
7.5	0.003374	0.007138	0.002201	0.0005995	0.0003379	0.01365
12.5	0.01863	0.04568	0.0161	0.007029	0.000197	0.08763
17.5	0.007186	0.01905	0.004592	0.00192	0.0001877	0.03294
22.5	0.0009872	0.002387	8.489e-05	0	0	0.00346
27.5	0	0	0	0	0	0
>30	0	0	0	0	0	0
Σ	0.03033	0.07462	0.02307	0.009561	0.0007227	0.1383

RR [mm h⁻¹]

F [-], ASPIRE (meso-scale) GEHALX 2022 (n = 2090)

WS [m s⁻¹]	0.5	3	7.5	15	>20	Σ
2.5	0.0002941	0.001223	0	0	0	0.001517
7.5	0.004899	0.008229	0.0006993	0	0	0.01383
12.5	0.02334	0.02944	0.006259	0	0	0.05904
17.5	0.01039	0.02324	0.002568	0	0	0.03619
22.5	0.002761	0.0006579	0	0	0	0.003419
27.5	0	0	0	0	0	0
>30	0	0	0	0	0	0
Σ	0.04168	0.06278	0.009526	0	0	0.114

RR [mm h⁻¹]

F [-], ASPIRE (LES) GEHALX 2022 (n = 77626)

WS [m s⁻¹]	0.5	3	7.5	15	>20	Σ
2.5	0.00012	0.0002713	0.0001124	0.0001469	0	0.0006505
7.5	0.002884	0.006468	0.003652	0.002061	0.0005247	0.01559
12.5	0.01244	0.02608	0.01248	0.009986	0.002356	0.06335
17.5	0.008121	0.02247	0.008277	0.006838	0.003202	0.0489
22.5	0.002632	0.006832	0.000869	0.0009877	0.001242	0.01256
27.5	0	0	0	0	0	0
>30	0	0	0	0	0	0
Σ	0.0262	0.06212	0.02539	0.02002	0.007325	0.1411

RR [mm h⁻¹]

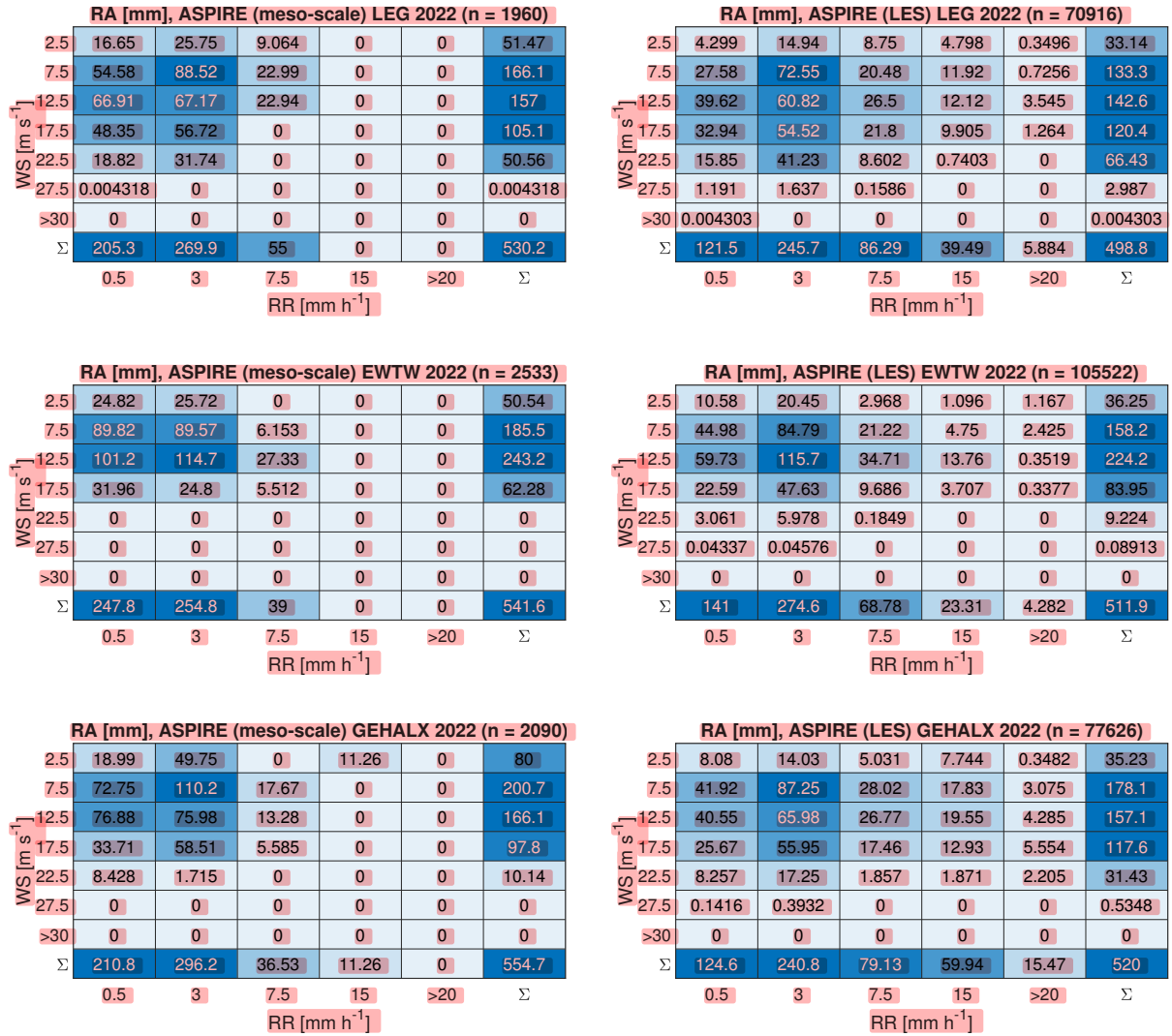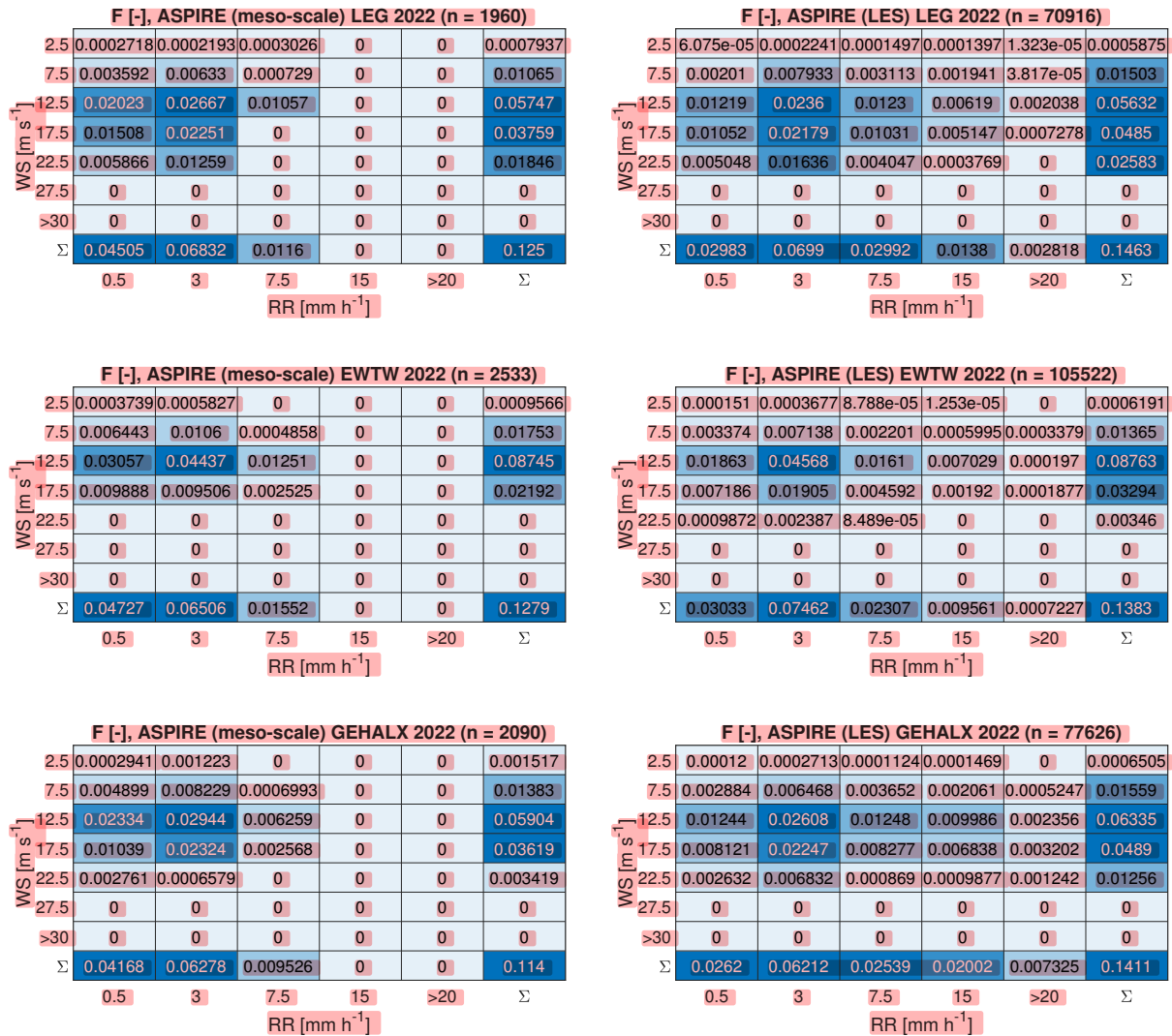**Figure 9.** Total annual damage classified into categories based on wind speed and rain rate. Presented here are the numerical results from meso-scale simulations and high resolution LES.

to other locations. It is possible that this discrepancy is related to the aforementioned uncertainties affecting disdrometer measurements. Compared to onshore locations, offshore and coastal environments are experimentally shown to experience more extreme rain events (Caboni et al., 2024; Hasager et al., 2020). This trend also appears to be captured by the simulations (see Figure 14).

270   In addition to extreme events, variations in DSD also contribute to differences in damage accumulation. The impact of these DSD differences is illustrated in Figure 16, which shows accumulated damage per unit of rainfall. The tables for each bin display the accumulated damage corresponding to every millimeter of rain that has fallen. It is noted that, within the same

Figure 10. Contour map of yearly accumulated damage based on one year of meso-scale simulations (right sub-plot) and high-resolution LES (left sub-plot).

categories, the observed accumulated damage per millimeter of rain exceeds the predictions made by the simulations. This discrepancy is linked to the DSD.

Figure 11. Contour map of yearly incubation period based on one year of meso-scale simulations (right sub-plot) and high-resolution LES (left sub-plot).

Figure 12. Contour map of yearly mean wind speed at 100 m above the ground and mean sea level based on one year of meso-scale simulations (right sub-plot) and high-resolution LES (left sub-plot).
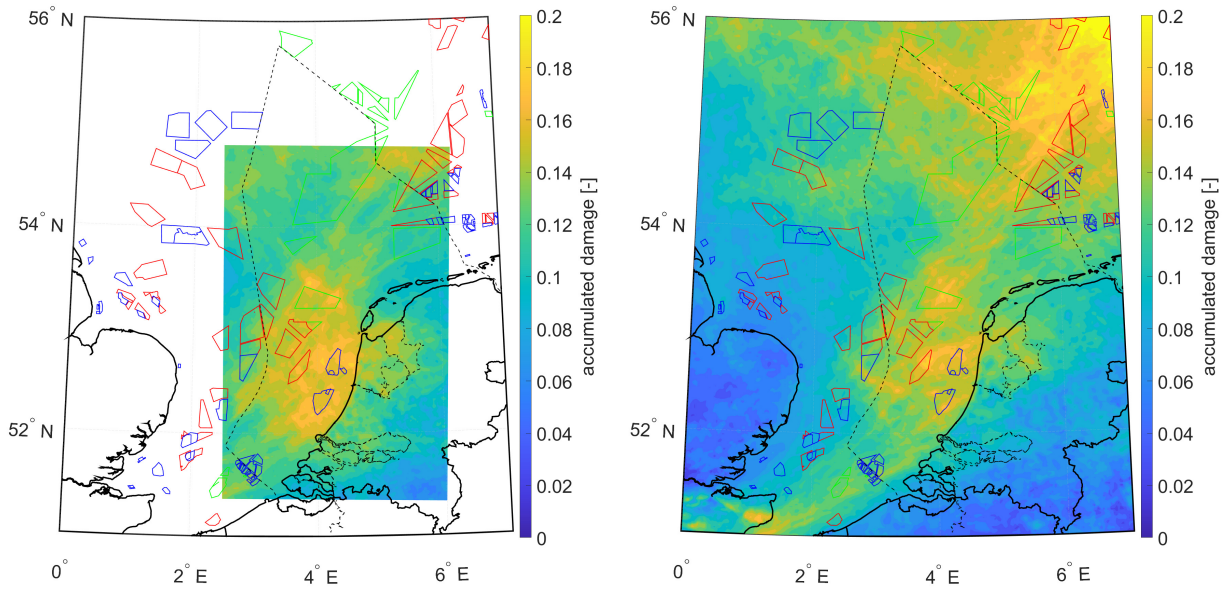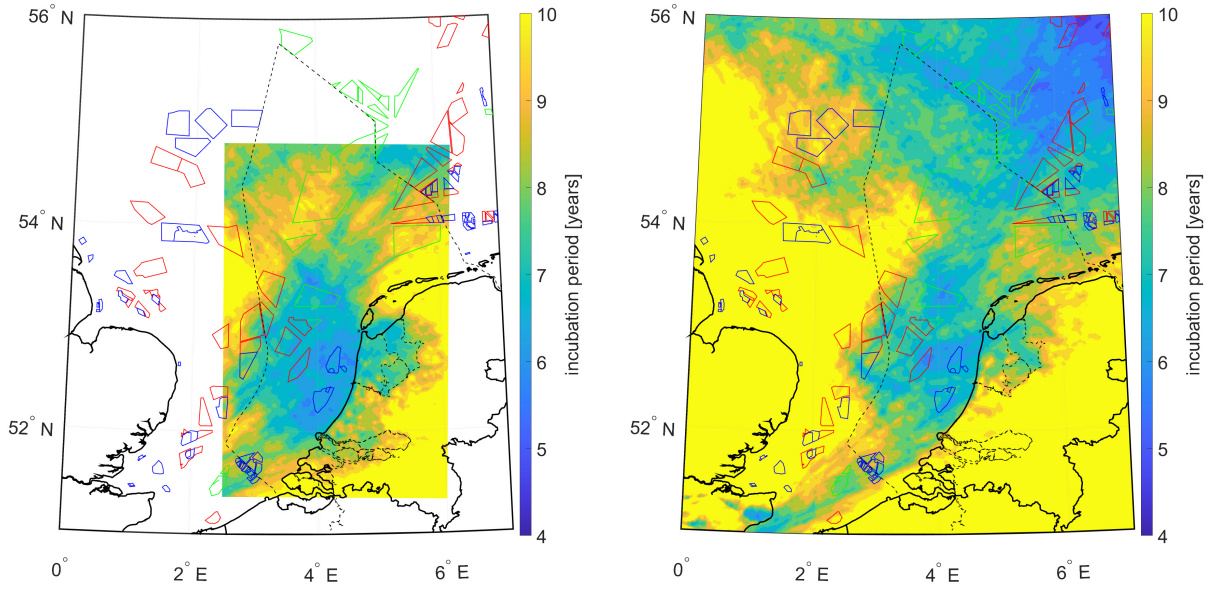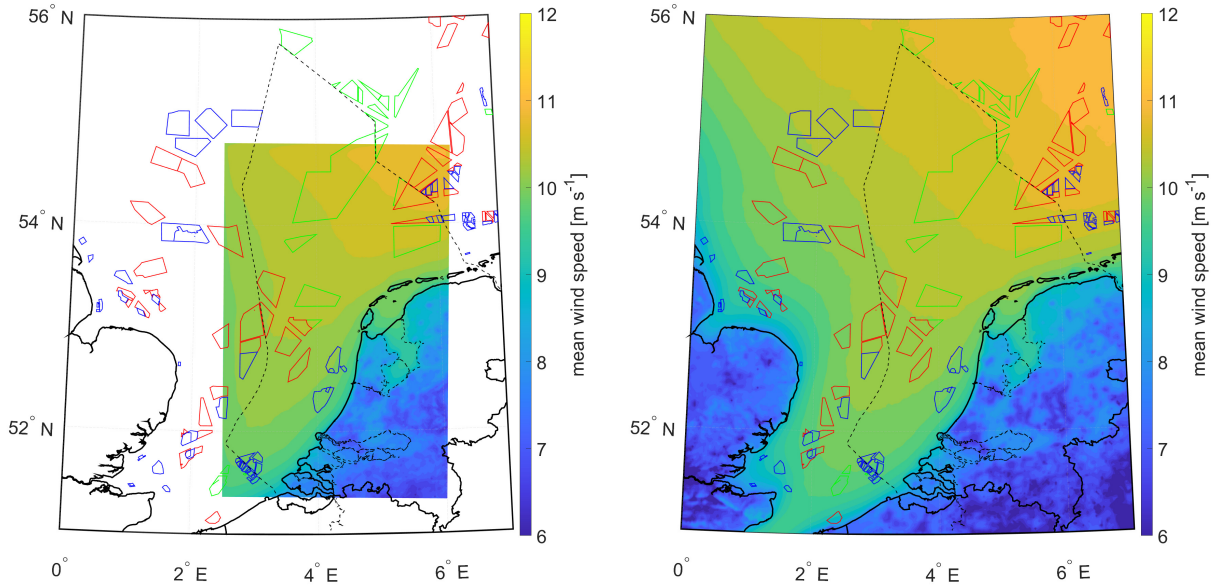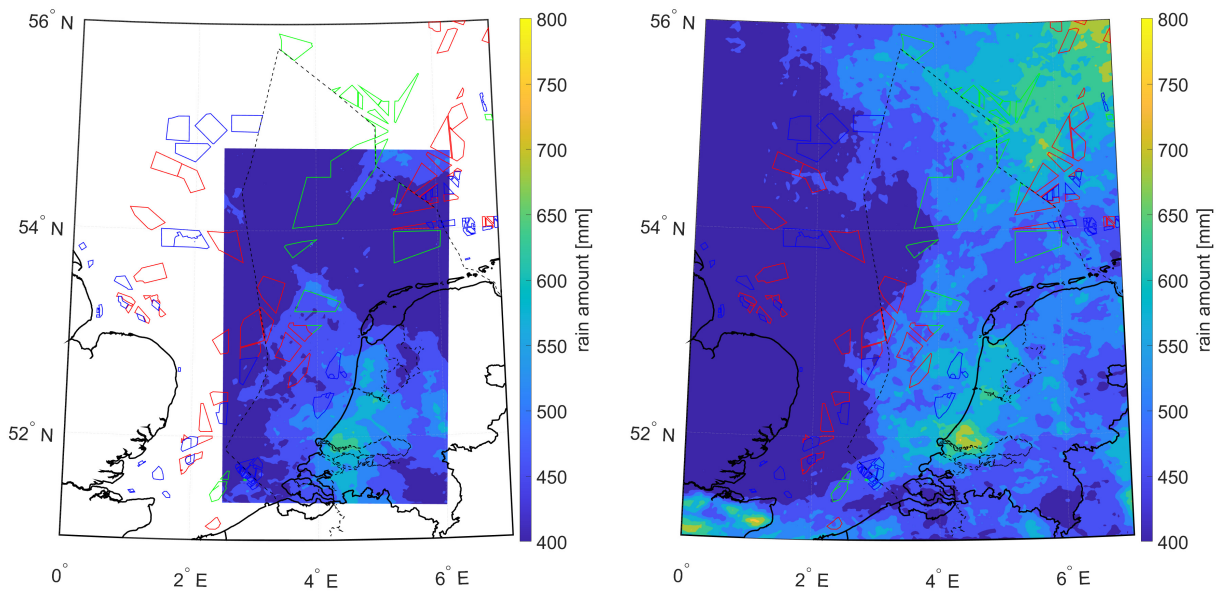
Figure 13. Contour map of yearly rain amount based on one year of meso-scale simulations (right sub-plot) and high-resolution LES (left sub-plot).

RA [mm], meas. LEG 2022 (n = 24541)

WS [m s⁻¹]	0.5	3	7.5	15	>20	Σ
2.5	9.928	18.35	6.987	7.867	17.93	61.06
7.5	31.89	54.49	18.37	13.05	7.036	124.8
12.5	21.29	55.67	26.7	23.69	23.43	150.8
17.5	14.5	44.39	32.66	35.16	19.03	145.7
22.5	7.387	23.58	16	20.39	2.662	70.02
27.5	0.3076	1.763	0.2039	0	0	2.275
>30	0	0	0	0	0	0
Σ	85.3	198.2	100.9	100.2	70.08	554.7

RR [mm h⁻¹]

RA [mm], ASPIRE (LES) LEG 2022 (n = 70916)

WS [m s⁻¹]	0.5	3	7.5	15	>20	Σ
2.5	4.299	14.94	8.75	4.798	0.3496	33.14
7.5	27.58	72.55	20.48	11.92	0.7256	133.3
12.5	39.62	60.82	26.5	12.12	3.545	142.6
17.5	32.94	54.52	21.8	9.905	1.264	120.4
22.5	15.85	41.23	8.602	0.7403	0	66.43
27.5	1.191	1.637	0.1586	0	0	2.987
>30	0.004303	0	0	0	0	0.004303
Σ	121.5	245.7	86.29	39.49	5.884	498.8

RR [mm h⁻¹]

RA [mm], meas. EWTW 2022 (n = 45558)

WS [m s⁻¹]	0.5	3	7.5	15	>20	Σ
2.5	21.03	58.28	22.62	11.02	3.735	116.7
7.5	60.94	137.8	46.12	18.9	5.434	269.2
12.5	40.03	90.75	23.83	13.25	3.775	171.6
17.5	8.222	18.14	2.101	0.8686	0	29.33
22.5	0.875	2.62	0.7243	0.2083	0	4.428
27.5	0.03058	0.02309	0	0	0	0.05367
>30	0.02065	0.02814	0	0	0	0.04879
Σ	131.1	307.7	95.39	44.24	12.94	591.4

RR [mm h⁻¹]

RA [mm], ASPIRE (LES) EWTW 2022 (n = 105522)

WS [m s⁻¹]	0.5	3	7.5	15	>20	Σ
2.5	10.58	20.45	2.968	1.096	1.167	36.25
7.5	44.98	84.79	21.22	4.75	2.425	158.2
12.5	59.73	115.7	34.71	13.76	0.3519	224.2
17.5	22.59	47.63	9.686	3.707	0.3377	83.95
22.5	3.061	5.978	0.1849	0	0	9.224
27.5	0.04337	0.04576	0	0	0	0.08913
>30	0	0	0	0	0	0
Σ	141	274.6	68.78	23.31	4.282	511.9

RR [mm h⁻¹]

RA [mm], meas. GEHALX 2022 (n = 28538)

WS [m s⁻¹]	0.5	3	7.5	15	>20	Σ
2.5	9.835	34.16	14.87	7.214	8.431	74.51
7.5	40.26	67.82	20.67	14.68	15.73	159.2
12.5	32.76	62.82	18.11	14.16	7.843	135.7
17.5	17.76	39.94	6.634	4.335	2.721	71.39
22.5	6.371	8.777	0.7887	0	0	15.94
27.5	0.074	0.06001	0	0	0	0.134
>30	0	0	0	0	0	0
Σ	107.1	213.6	61.07	40.39	34.72	456.8

RR [mm h⁻¹]

RA [mm], ASPIRE (LES) GEHALX 2022 (n = 77626)

WS [m s⁻¹]	0.5	3	7.5	15	>20	Σ
2.5	8.08	14.03	5.031	7.744	0.3482	35.23
7.5	41.92	87.25	28.02	17.83	3.075	178.1
12.5	40.55	65.98	26.77	19.55	4.285	157.1
17.5	25.67	55.95	17.46	12.93	5.554	117.6
22.5	8.257	17.25	1.857	1.871	2.205	31.43
27.5	0.1416	0.3932	0	0	0	0.5348
>30	0	0	0	0	0	0
Σ	124.6	240.8	79.13	59.94	15.47	520

RR [mm h⁻¹]

Figure 14. Annual rainfall categorized into bins based on wind speed and rain rate. Presented here are the numerical results from the high resolution LES.
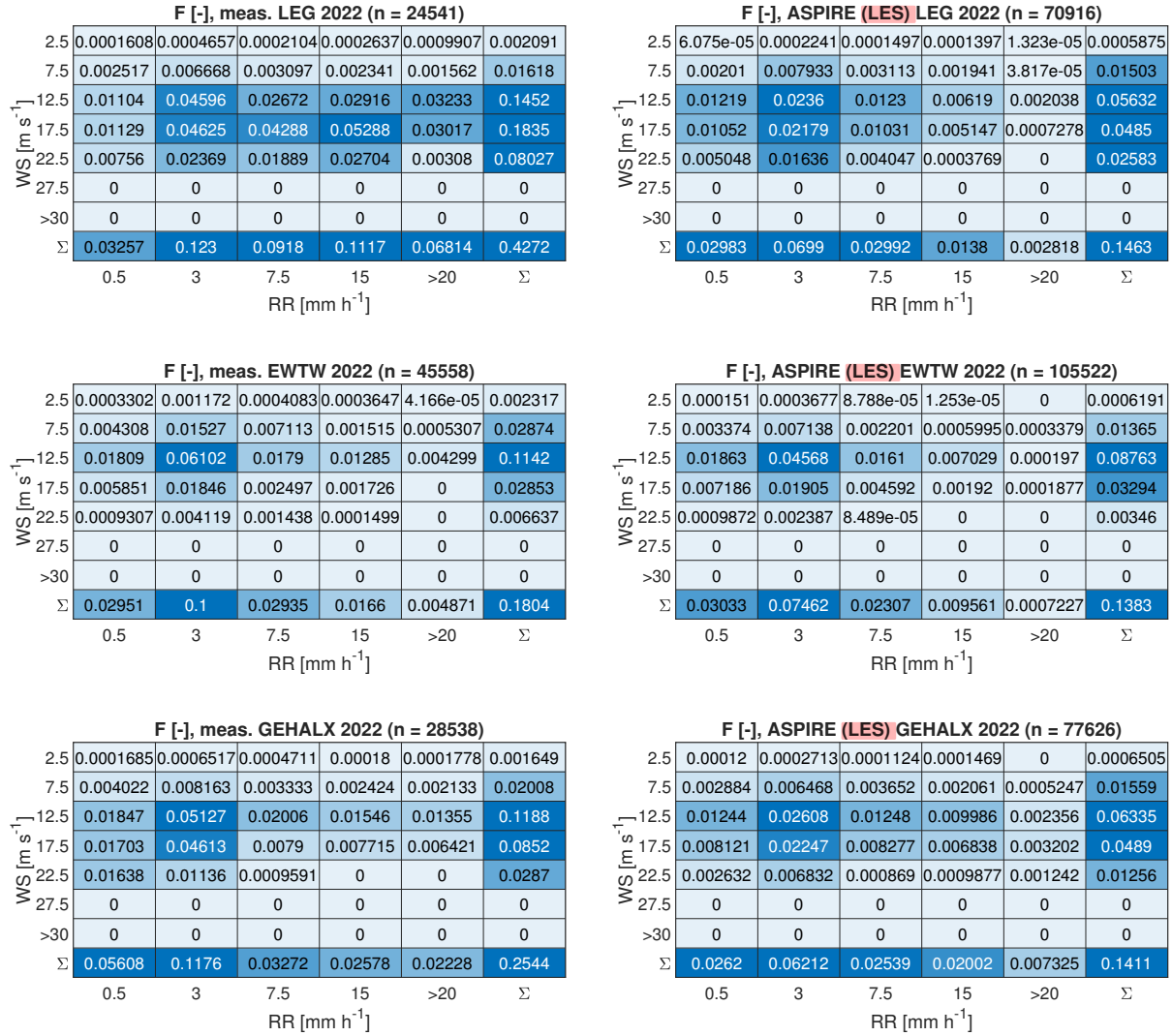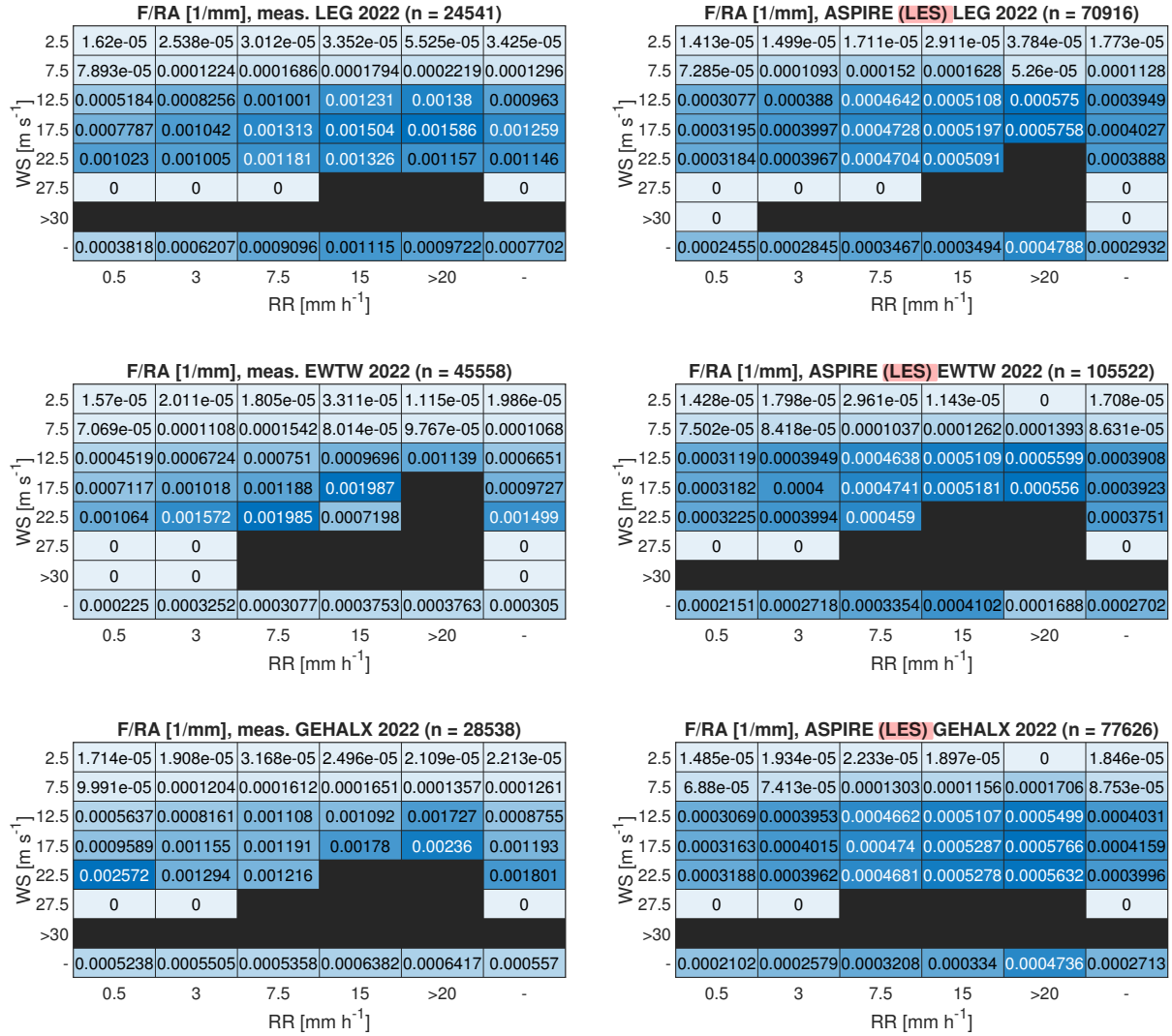
F [-], meas. LEG 2022 (n = 24541)

WS [m s^{-1}] \ RR [mm h^{-1}]	0.5	3	7.5	15	>20	Σ
2.5	0.0001608	0.0004657	0.0002104	0.0002637	0.0009907	0.002091
7.5	0.002517	0.006668	0.003097	0.002341	0.001562	0.01618
12.5	0.01104	0.04596	0.02672	0.02916	0.03233	0.1452
17.5	0.01129	0.04625	0.04288	0.05288	0.03017	0.1835
22.5	0.00756	0.02369	0.01889	0.02704	0.00308	0.08027
27.5	0	0	0	0	0	0
>30	0	0	0	0	0	0
Σ	0.03257	0.123	0.0918	0.1117	0.06814	0.4272

F [-], ASPIRE (LES) LEG 2022 (n = 70916)

WS [m s^{-1}] \ RR [mm h^{-1}]	0.5	3	7.5	15	>20	Σ
2.5	6.075e-05	0.0002241	0.0001497	0.0001397	1.323e-05	0.0005875
7.5	0.00201	0.007933	0.003113	0.001941	3.817e-05	0.01503
12.5	0.01219	0.0236	0.0123	0.00619	0.002038	0.05632
17.5	0.01052	0.02179	0.01031	0.005147	0.0007278	0.0485
22.5	0.005048	0.01636	0.004047	0.0003769	0	0.02583
27.5	0	0	0	0	0	0
>30	0	0	0	0	0	0
Σ	0.02983	0.0699	0.02992	0.0138	0.002818	0.1463

F [-], meas. EWTW 2022 (n = 45558)

WS [m s^{-1}] \ RR [mm h^{-1}]	0.5	3	7.5	15	>20	Σ
2.5	0.0003302	0.001172	0.0004083	0.0003647	4.166e-05	0.002317
7.5	0.004308	0.01527	0.007113	0.001515	0.0005307	0.02874
12.5	0.01809	0.06102	0.0179	0.01285	0.004299	0.1142
17.5	0.005851	0.01846	0.002497	0.001726	0	0.02853
22.5	0.0009307	0.004119	0.001438	0.0001499	0	0.006637
27.5	0	0	0	0	0	0
>30	0	0	0	0	0	0
Σ	0.02951	0.1	0.02935	0.0166	0.004871	0.1804

F [-], ASPIRE (LES) EWTW 2022 (n = 105522)

WS [m s^{-1}] \ RR [mm h^{-1}]	0.5	3	7.5	15	>20	Σ
2.5	0.000151	0.0003677	8.788e-05	1.253e-05	0	0.0006191
7.5	0.003374	0.007138	0.002201	0.0005995	0.0003379	0.01365
12.5	0.01863	0.04568	0.0161	0.007029	0.000197	0.08763
17.5	0.007186	0.01905	0.004592	0.00192	0.0001877	0.03294
22.5	0.0009872	0.002387	8.489e-05	0	0	0.00346
27.5	0	0	0	0	0	0
>30	0	0	0	0	0	0
Σ	0.03033	0.07462	0.02307	0.009561	0.0007227	0.1383

F [-], meas. GEHALX 2022 (n = 28538)

WS [m s^{-1}] \ RR [mm h^{-1}]	0.5	3	7.5	15	>20	Σ
2.5	0.0001685	0.0006517	0.0004711	0.00018	0.0001778	0.001649
7.5	0.004022	0.008163	0.003333	0.002424	0.002133	0.02008
12.5	0.01847	0.05127	0.02006	0.01546	0.01355	0.1188
17.5	0.01703	0.04613	0.0079	0.007715	0.006421	0.0852
22.5	0.01638	0.01136	0.0009591	0	0	0.0287
27.5	0	0	0	0	0	0
>30	0	0	0	0	0	0
Σ	0.05608	0.1176	0.03272	0.02578	0.02228	0.2544

F [-], ASPIRE (LES) GEHALX 2022 (n = 77626)

WS [m s^{-1}] \ RR [mm h^{-1}]	0.5	3	7.5	15	>20	Σ
2.5	0.00012	0.0002713	0.0001124	0.0001469	0	0.0006505
7.5	0.002884	0.006468	0.003652	0.002061	0.0005247	0.01559
12.5	0.01244	0.02608	0.01248	0.009986	0.002356	0.06335
17.5	0.008121	0.02247	0.008277	0.006838	0.003202	0.0489
22.5	0.002632	0.006832	0.000869	0.0009877	0.001242	0.01256
27.5	0	0	0	0	0	0
>30	0	0	0	0	0	0
Σ	0.0262	0.06212	0.02539	0.02002	0.007325	0.1411

Figure 15. Total annual damage classified into categories based on wind speed and rain rate. Presented here are the numerical results from the high resolution LES.

F/RA [1/mm], meas. LEG 2022 (n = 24541)

WS [m s⁻¹] \ RR [mm h⁻¹]	0.5	3	7.5	15	>20	-
2.5	1.62e-05	2.538e-05	3.012e-05	3.352e-05	5.525e-05	3.425e-05
7.5	7.893e-05	0.0001224	0.0001686	0.0001794	0.0002219	0.0001296
12.5	0.0005184	0.0008256	0.001001	0.001231	0.00138	0.000963
17.5	0.0007787	0.001042	0.001313	0.001504	0.001586	0.001259
22.5	0.001023	0.001005	0.001181	0.001326	0.001157	0.001146
27.5	0	0	0			0
>30						0
-	0.0003818	0.0006207	0.0009096	0.001115	0.0009722	0.0007702

F/RA [1/mm], ASPIRE (LES) LEG 2022 (n = 70916)

WS [m s⁻¹] \ RR [mm h⁻¹]	0.5	3	7.5	15	>20	-
2.5	1.413e-05	1.499e-05	1.711e-05	2.911e-05	3.784e-05	1.773e-05
7.5	7.285e-05	0.0001093	0.000152	0.0001628	5.26e-05	0.0001128
12.5	0.0003077	0.000388	0.0004642	0.0005108	0.000575	0.0003949
17.5	0.0003195	0.0003997	0.0004728	0.0005197	0.0005758	0.0004027
22.5	0.0003184	0.0003967	0.0004704	0.0005091		0.0003888
27.5	0	0	0			0
>30	0					0
-	0.0002455	0.0002845	0.0003467	0.0003494	0.0004788	0.0002932

F/RA [1/mm], meas. EWTW 2022 (n = 45558)

WS [m s⁻¹] \ RR [mm h⁻¹]	0.5	3	7.5	15	>20	-
2.5	1.57e-05	2.011e-05	1.805e-05	3.311e-05	1.115e-05	1.986e-05
7.5	7.069e-05	0.0001108	0.0001542	8.014e-05	9.767e-05	0.0001068
12.5	0.0004519	0.0006724	0.000751	0.0009696	0.001139	0.0006651
17.5	0.0007117	0.001018	0.001188	0.001987		0.0009727
22.5	0.001064	0.001572	0.001985	0.0007198		0.001499
27.5	0	0				0
>30	0	0				0
-	0.000225	0.0003252	0.0003077	0.0003753	0.0003763	0.000305

F/RA [1/mm], ASPIRE (LES) EWTW 2022 (n = 105522)

WS [m s⁻¹] \ RR [mm h⁻¹]	0.5	3	7.5	15	>20	-
2.5	1.428e-05	1.798e-05	2.961e-05	1.143e-05	0	1.708e-05
7.5	7.502e-05	8.418e-05	0.0001037	0.0001262	0.0001393	8.631e-05
12.5	0.0003119	0.0003949	0.0004638	0.0005109	0.0005599	0.0003908
17.5	0.0003182	0.0004	0.0004741	0.0005181	0.000556	0.0003923
22.5	0.0003225	0.0003994	0.000459			0.0003751
27.5	0	0				0
>30						
-	0.0002151	0.0002718	0.0003354	0.0004102	0.0001688	0.0002702

F/RA [1/mm], meas. GEHALX 2022 (n = 28538)

WS [m s⁻¹] \ RR [mm h⁻¹]	0.5	3	7.5	15	>20	-
2.5	1.714e-05	1.908e-05	3.168e-05	2.496e-05	2.109e-05	2.213e-05
7.5	9.991e-05	0.0001204	0.0001612	0.0001651	0.0001357	0.0001261
12.5	0.0005637	0.0008161	0.001108	0.001092	0.001727	0.0008755
17.5	0.0009589	0.001155	0.001191	0.00178	0.00236	0.001193
22.5	0.002572	0.001294	0.001216			0.001801
27.5	0	0				0
>30						
-	0.0005238	0.0005505	0.0005358	0.0006382	0.0006417	0.000557

F/RA [1/mm], ASPIRE (LES) GEHALX 2022 (n = 77626)

WS [m s⁻¹] \ RR [mm h⁻¹]	0.5	3	7.5	15	>20	-
2.5	1.485e-05	1.934e-05	2.233e-05	1.897e-05	0	1.846e-05
7.5	6.88e-05	7.413e-05	0.0001303	0.0001156	0.0001706	8.753e-05
12.5	0.0003069	0.0003953	0.0004662	0.0005107	0.0005499	0.0004031
17.5	0.0003163	0.0004015	0.000474	0.0005287	0.0005766	0.0004159
22.5	0.0003188	0.0003962	0.0004681	0.0005278	0.0005632	0.0003996
27.5	0	0				0
>30						
-	0.0002102	0.0002579	0.0003208	0.000334	0.0004736	0.0002713

Figure 16. Yearly accumulated damage per rain amount sorted out into wind speed and rain rate bins. Presented here are the numerical results from the high resolution LES.

275 Figure 17 shows the comparison between the measured and simulated DSD at the three locations, for a fixed rain rate and varying wind speeds. As mentioned above, the simulations assume a DSD based on a Marshall-Palmer distribution. The comparison shows that the Marshall-Palmer distribution matches the measured DSD for drop sizes up to approximately 3 mm. Beyond this size, the Marshall-Palmer distribution significantly underestimates the droplet amount. This difference becomes more pronounced as the wind speed increases. Indeed, the measurements clearly indicate that wind speed influences

280 the DSD. At higher wind speeds, a greater number of relatively large droplets are observed. Similar results were also observed by Montero-Martínez and García-García (2016) and Thurai et al. (2019).
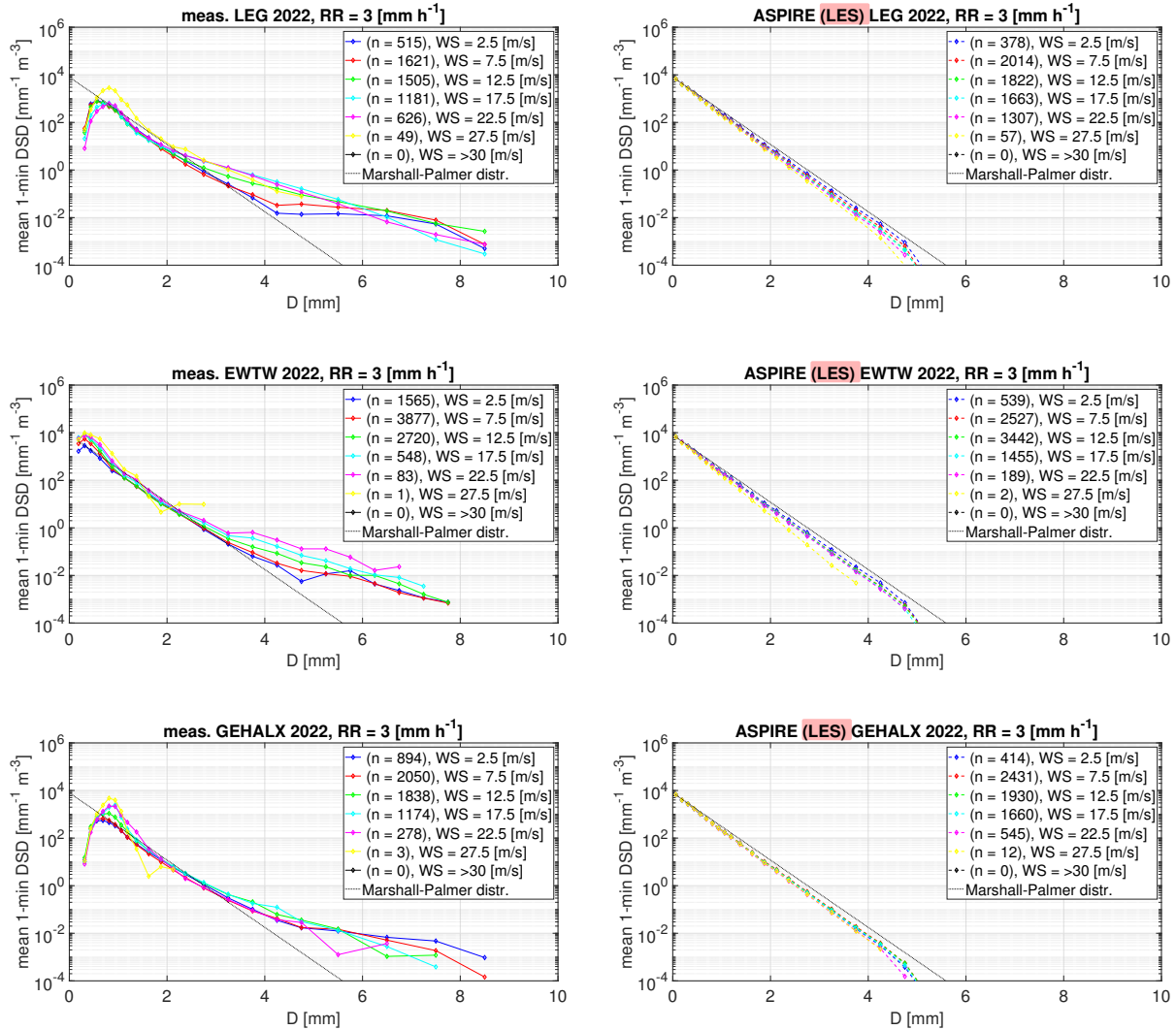
Figure 17. Mean drop size distributions for a fixed rain rate of 3 mm h^{-1} and different wind speeds. ASPIRE's results are here derived from the LES data.

To finalize the comparison between observations and simulations, we also include the drop fall velocity. Figure 18 presents the comparison between the measured and simulated drop fall velocities at the three locations, for a fixed rain rate and different wind speeds. Concerning fall velocity, the approximation used in ASPIRE is based on a simple model provided by Lin et al.

285 (1983). The approximation by Lin et al. (1983) aligns well with measurements for droplets with diameters of up to 2 mm. Beyond this value, the measurements show a constant falling speed, whereas Lin et al. (1983)'s approximation assumes that the fall velocity increases. Similar to the DSD, the measured fall speed also appears to vary with wind speed, showing lower fall speeds at higher wind velocities.
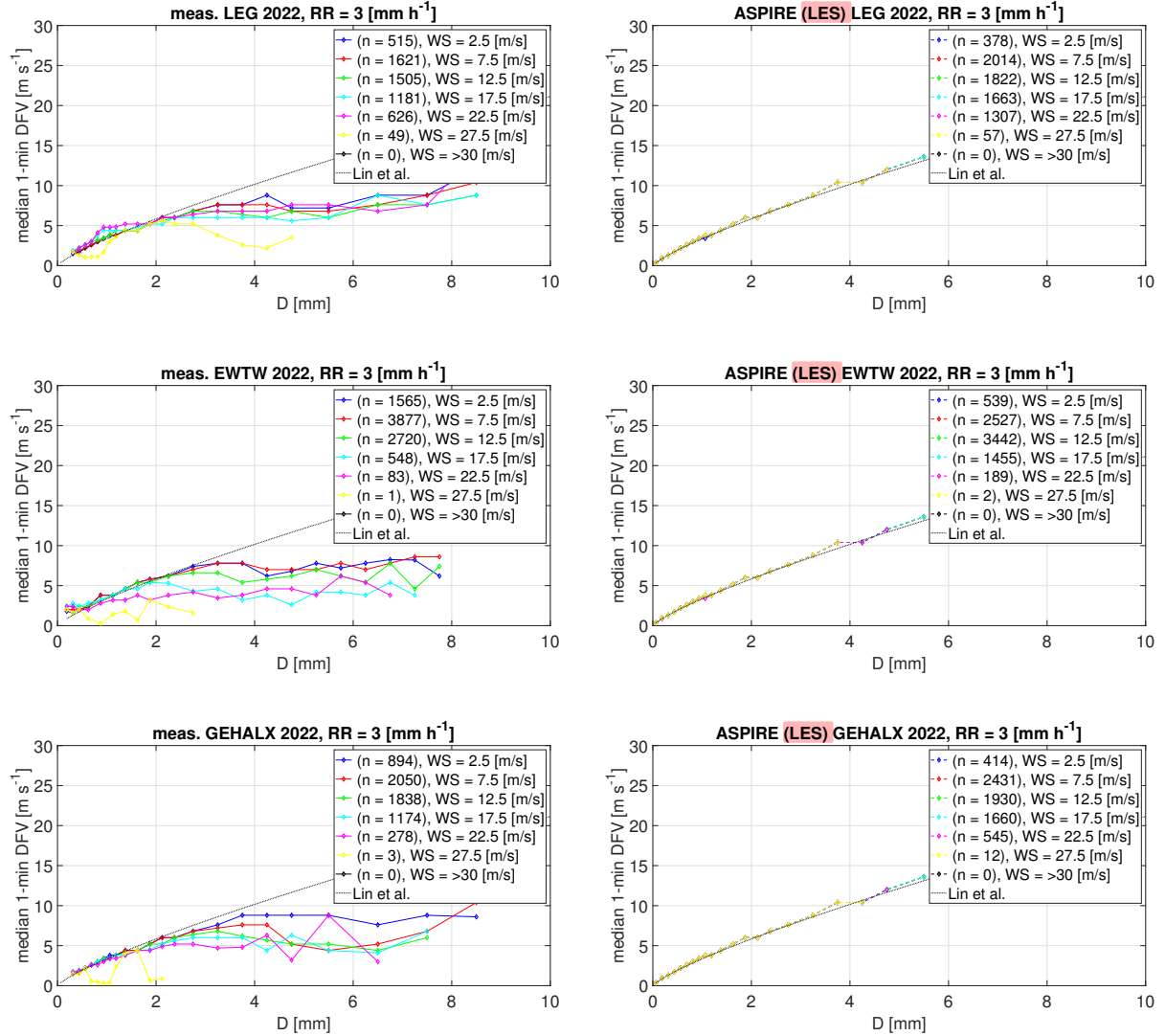
Figure 18. Median drop fall velocity for a fixed rain rate of 3 mm h^{-1} and different wind speeds. ASPIRE's results are here derived from the LES data.

25

4 Discussions

By conducting 10-year long meso-scale simulations to account for long-term climatology, our study has highlighted the variation of rain-induced erosivity across the Dutch North Sea. Examining the portion of the Dutch North Sea covered in the reanalysis-based erosion atlas by Hannesdóttir et al. (2024b), no clear trends can be inferred within this region. This is because their atlas focuses on Scandinavian regions and only marginally and partially covers the Dutch North Sea. According to this atlas, the incubation period is approximately 4 years over the covered Dutch North Sea, which is about 40% lower than the incubation period resulting from our meso-scale based erosion atlas. These differences can be attributed not only to the weather model with specific resolutions and periods but also to assumptions regarding DSD, drop falling speed, damage model, and fatigue characteristics of the LEP system. Such assumptions have a dramatic effect on the resulting incubation period. Due to the complexity of the calculations behind an erosion atlas, considering the assumptions and models used to generate it, it is not possible to detail where the differences between our atlas and the one by Hannesdóttir et al. (2024b) come from. Future research should aim at dedicated comparisons of erosion atlases, systematically breaking down the calculation chain and comparing results for each portion.

Our study indicates that a LES setup with finer spatial and temporal resolution enhances the ability of simulations to capture more extreme events. This is because the smaller temporal resolution allows the simulations to detect more short-term extreme events with high rain intensity. Such high-intensity events contain larger and more erosive droplets. With larger temporal resolutions, these events are averaged out. Our comparative analysis with actual measurements reveals that both meso-scale and LES models tend to underpredict the accumulated damage. One reason is that the Marshall-Palmer distribution assumed by both numerical models significantly underestimates the amount of large droplets compared to what is measured. Another reason is that more extreme events are recorded than those simulated, especially at the instrumented offshore location. Significant uncertainties still exist in detecting such events in both measurements and simulations. Detailed measurements of rain in offshore locations are new, and further research is required to improve these measurements and establish confidence bounds.

As previously mentioned, the estimates of incubation periods provided by this study, whether derived from measurements or simulations, are based on various methods and several assumptions. Unfortunately, these estimates have not been validated in real-world conditions yet. However, we can say that these figures are roughly in line with the leading edge repair interventions of wind turbines in the Dutch North Sea.

5 Conclusions

Meso-scale simulations carried out over a decade showed that the average erosivity of rainfall on wind turbine blades increases from the southwestern part of the Dutch North Sea to the northeastern region. Indeed, the simulations indicate that the northeastern regions are characterized by both higher average wind speeds and a larger amount of rainfall. These results suggest that future wind farms developed in the northeast are likely to encounter higher erosion rates compared to those currently operating in the southwest. This requires special attention when developing mitigation strategies, such as the development of advanced leading-edge protection systems, the implementation of effective maintenance practices for erosion prevention,

and the application of erosion-safe modes, which involve reducing rotor speed during extreme events to prolong the blades' lifespan.

A year-long comparison of meso-scale simulations and high-resolution large eddy simulations (LES) showed that the accumulated damage estimated from meso-scale simulations is 7 to 20% lower than that obtained from LES. These differences can be attributed to the LES setup's ability to capture more extreme events due to its finer spatial and temporal resolution. However, a side-by-side comparison of the contour maps obtained using meso-scale simulations and LES reveals alignment in the spatial patterns of erosion-related parameters, confirming that meso-scale simulations produce satisfactory atlases where regional differences are consistently captured with LES. Additionally, a comparison of LES and measurements at selected sites in The Netherlands over a one-year period revealed that the accumulated damage estimated from simulations is 23 to 66% lower than that obtained from actual weather data. These differences can be attributed to two main factors. Firstly, there are more extreme events recorded than those predicted by LES. Secondly, the Marshall-Palmer distribution, assumed by the simulations, tends to underestimate the quantity of larger droplets. Together, these factors result in simulations predicting less accumulated damage.

Future work will involve implementing a more representative drop size distribution and fall velocity in the weather model. In this context, models will need to be validated with more reliable measurements, which is also a topic of ongoing and future research. To mitigate erosion on wind turbines, high resolution weather models could be employed to investigate a now-cast based erosion-safe mode, where the model could forecast extreme events, enabling operators to adjust rotor speed accordingly.

350

References

Baas, P., Verzijlbergh, R., van Dorp, P., and Jonker, H.: Investigating energy production and wake losses of multi-gigawatt offshore wind farms with atmospheric large-eddy simulation, Wind Energy Science, 8, 787–805, https://doi.org/10.5194/wes-8-787-2023, 2023.

355 Bak, C., Forsting, A. M., and Sorensen, N. N.: The influence of leading edge roughness, rotor control and wind climate on the loss in energy production, Journal of Physics: Conference Series, 1618, 052 050, https://doi.org/10.1088/1742-6596/1618/5/052050, 2020.

Barfknecht, N. and von Terzi, D.: On the significance of rain droplet slowdown and deformation for leading-edge rain erosion, Wind Energy Science Discussions, 2023, 1–42, https://doi.org/10.5194/wes-2023-169, 2023.

Barfknecht, N. and von Terzi, D.: Drop-size-dependent effects in leading-edge rain erosion and their impact for erosion-safe mode operation,
360 Wind Energy Science Discussions, 2024, 1–49, https://doi.org/10.5194/wes-2024-33, 2024.

Caboni, M., Slot, H. M., Bergman, G., Wouters, D. A. J., and Meijer, H. J. V. D. M.: Evaluation of wind turbine blades' rain-induced leading edge erosion using rainfall measurements at offshore, coastal and onshore locations in the Netherlands, Journal of Physics: Conference Series, 2767, 062 003, https://doi.org/10.1088/1742-6596/2767/6/062003, 2024.

Caboni, M., Schwarz, A., Slot, H., and van der Mijle Meijer, H.: Estimating microplastics emissions from offshore wind turbines in the Dutch
365 North Sea, in preparation, 2025.

Castorrini, A., Ortolani, A., and Campobasso, M. S.: Assessing the progression of wind turbine energy yield losses due to blade erosion by resolving damage geometries from lab tests and field observations, Renewable Energy, 218, 119 256, https://doi.org/10.1016/j.renene.2023.119256, 2023.

Copernicus-Climate-Change-Service: Copernicus Interactive Climate Atlas, https://atlas.climate.copernicus.eu/atlas, accessed: 2024-12-02.

370 Davis, N. N., Badger, J., Hahmann, A. N., Hansen, B. O., Mortensen, N. G., Kelly, M., Larsén, X. G., Olsen, B. T., Floors, R., Lizcano, G., Casso, P., Lacave, O., Bosch, A., Bauwens, I., Knight, O. J., van Loon, A. P., Fox, R., Parvanyan, T., Hansen, S. B. K., Heathfield, D., Onninen, M., and Drummond, R.: The Global Wind Atlas: A High-Resolution Dataset of Climatologies and Associated Web-Based Application, Bulletin of the American Meteorological Society, 104, E1507 – E1525, https://doi.org/10.1175/BAMS-D-21-0075.1, 2023.

Gaertner, E., Rinker, J., Sethuraman, L., Zahle, F., Anderson, B., Barter, G., Abbas, N., Meng, F., Bortolotti, P., Skrzypinski, W.,
375 Scott, G., Feil, R., Bredmose, H., Dykes, K., Shields, M., Allen, C., and Viselli, A.: Definition of the IEA 15-Megawatt Offshore Reference Wind Turbine, Tech. Rep. NREL/TP-5000-75698, National Renewable Energy Laboratory (NREL), Golden, CO, USA, https://doi.org/10.2172/1603478, 2020.

Grabowski, W. W.: Toward Cloud Resolving Modeling of Large-Scale Tropical Circulations: A Simple Cloud Microphysics Parameterization, Journal of the Atmospheric Sciences, 55, 3283 – 3298, https://doi.org/10.1175/1520-0469(1998)055<3283:TCRMOL>2.0.CO;2, 1998.

380 Hahmann, A. N., Sīle, T., Witha, B., Davis, N. N., Dörenkämper, M., Ezber, Y., García-Bustamante, E., González-Rouco, J. F., Navarro, J., Olsen, B. T., and Söderberg, S.: The making of the New European Wind Atlas – Part 1: Model sensitivity, Geoscientific Model Development, 13, 5053–5078, https://doi.org/10.5194/gmd-13-5053-2020, 2020.

Hannesdóttir, A., Dellwik, E., and Hasager, C. B.: Prediction of rain erosion damage progression using disdrometer rain data: The importance of liquid water content, Journal of Physics: Conference Series, 2767, 042 024, https://doi.org/10.1088/1742-6596/2767/4/042024, 2024a.

385 Hannesdóttir, A., Kral, S. T., Reuder, J., and Hasager, C. B.: Rain erosion atlas for wind turbine blades based on ERA5 and NORA3 for Scandinavia, Results in Engineering, 22, 102 010, https://doi.org/10.1016/j.rineng.2024.102010, 2024b.

Hasager, C., Vejen, F., Bech, J., Skrzypiński, W., Tilg, A.-M., and Nielsen, M.: Assessment of the rain and wind climate with focus on wind turbine blade leading edge erosion rate and expected lifetime in Danish Seas, Renewable Energy, 149, 91–102, https://doi.org/10.1016/j.renene.2019.12.043, 2020.

390 Hasager, C. B., Vejen, F., Skrzypiński, W. R., and Tilg, A.-M.: Rain Erosion Load and Its Effect on Leading-Edge Lifetime and Potential of Erosion-Safe Mode at Wind Turbines in the North Sea and Baltic Sea, Energies, 14, https://doi.org/10.3390/en14071959, 2021.

Hersbach, H., Bell, B., Berrisford, P., Hirahara, S., Horányi, A., Muñoz-Sabater, J., Nicolas, J., Peubey, C., Radu, R., Schepers, D., Simmons, A., Soci, C., Abdalla, S., Abellan, X., Balsamo, G., Bechtold, P., Biavati, G., Bidlot, J., Bonavita, M., De Chiara, G., Dahlgren, P., Dee, D., Diamantakis, M., Dragani, R., Flemming, J., Forbes, R., Fuentes, M., Geer, A., Haimberger, L., Healy, S., Hogan, R. J.,

395 Hólm, E., Janisková, M., Keeley, S., Laloyaux, P., Lopez, P., Lupu, C., Radnoti, G., de Rosnay, P., Rozum, I., Vamborg, F., Villaume, S., and Thépaut, J.-N.: The ERA5 global reanalysis, Quarterly Journal of the Royal Meteorological Society, 146, 1999–2049, https://doi.org/10.1002/qj.3803, 2020.

Heus, T., van Heerwaarden, C. C., Jonker, H. J. J., Pier Siebesma, A., Axelsen, S., van den Dries, K., Geoffroy, O., Moene, A. F., Pino, D., de Roode, S. R., and Vilà-Guerau de Arellano, J.: Formulation of the Dutch Atmospheric Large-Eddy Simulation (DALES) and overview

400 of its applications, Geoscientific Model Development, 3, 415–444, https://doi.org/10.5194/gmd-3-415-2010, 2010.

Heymann, F. J.: Conclusions from the ASTM interlaboratory test program with liquid impact erosion facilities, in: In: International Conference on Erosion by Liquid and Solid Impact, pp. 1–10, 1979.

Larsén, X. G., Davis, N., Hannesdóttir, A., Kelly, M., Svenningsen, L., Slot, R., Imberger, M., Olsen, B. T., and Floors, R.: The Global Atlas for Siting Parameters project: Extreme wind, turbulence, and turbine classes, Wind Energy, 25, 1841–1859,

405 https://doi.org/10.1002/we.2771, 2022.

Letson, F. and Pryor, S. C.: From Hydrometeor Size Distribution Measurements to Projections of Wind Turbine Blade Leading-Edge Erosion, Energies, 16, https://doi.org/10.3390/en16093906, 2023.

Lin, Y.-L., Farley, R. D., and Orville, H. D.: Bulk Parameterization of the Snow Field in a Cloud Model, Journal of Applied Meteorology and Climatology, 22, 1065 – 1092, https://doi.org/10.1175/1520-0450(1983)022<1065:BPOTSF>2.0.CO;2, 1983.

410 Maniaci, D. C., Westergaard, C., Hsieh, A., and Paquette, J. A.: Uncertainty Quantification of Leading Edge Erosion Impacts on Wind Turbine Performance, Journal of Physics: Conference Series, 1618, 052 082, https://doi.org/10.1088/1742-6596/1618/5/052082, 2020.

Marshall, J. S. and Palmer, W. M. K.: THE DISTRIBUTION OF RAINDROPS WITH SIZE, Journal of Atmospheric Sciences, 5, 165 – 166, https://doi.org/10.1175/1520-0469(1948)005<0165:TDORWS>2.0.CO;2, 1948.

Mishnaevsky, L.: Repair of wind turbine blades: Review of methods and related computational mechanics problems, Renewable Energy, 140,

415 828–839, https://doi.org/10.1016/j.renene.2019.03.113, 2019.

Mishnaevsky, L., Hasager, C. B., Bak, C., Tilg, A.-M., Bech, J. I., Doagou Rad, S., and Fæster, S.: Leading edge erosion of wind turbine blades: Understanding, prevention and protection, Renewable Energy, 169, 953–969, https://doi.org/10.1016/j.renene.2021.01.044, 2021.

Montero-Martínez, G. and García-García, F.: On the behaviour of raindrop fall speed due to wind, Quarterly Journal of the Royal Meteorological Society, 142, 2013–2020, https://doi.org/10.1002/qj.2794, 2016.

420 Mortensen, N., Hansen, J., Kelly, M., Prinsloo, E., Mabille, E., and Szewczuk, S.: Wind Atlas for South Africa (WASA) Station and Site Description Report, no. 0242(EN) in DTU Wind Energy I, DTU Wind Energy, Denmark, for an electronic copy please contact the first author. Published as DTU Wind Energy E-0071 in 2014., 2014.

Méndez, B., Saenz, E., Óscar Pires, Cantero, E., Bech, J., Polls, F., Peinó, E., Udina, M., and Garcia-Benadí, A.: Experimental campaign for the characterization of precipitation in a complex terrain site using high resolution observations, Journal of Physics: Conference Series, 2767, 042 016, https://doi.org/10.1088/1742-6596/2767/4/042016, 2024.

Nawri, N., Petersen, G. N., Bjornsson, H., Hahmann, A. N., Jónasson, K., Hasager, C. B., and Clausen, N.-E.: The wind energy potential of Iceland, Renewable Energy, 69, 290–299, https://doi.org/10.1016/j.renene.2014.03.040, 2014.

Noordzeeloket: Energy Transition in the North Sea, https://www.noordzeeloket.nl/en/functions-and-use/offshore-wind-energy/energy-transition-north-sea/, accessed: 2024-12-06, 2024.

North-Sea-Energy: Offshore Renewables - Offshore Wind Visibility, https://northseaenergy.projectatlas.app/atlas/offshore-renewables-offshore-wind/visibility?map=53.01448,4.36442,6.18,0,0&ds=6344220c36f492e236880e70&list=wind-potential-map, accessed: 2024-11-30, 2024.

Pryor, S. C., Letson, F., Shepherd, T., and Barthelmie, R. J.: Evaluation of WRF Simulation of Deep Convection in the U.S. Southern Great Plains, Journal of Applied Meteorology and Climatology, 62, 41 – 62, https://doi.org/10.1175/JAMC-D-22-0090.1, 2023.

Pryor, S. C., Barthelmie, R. J., and Hannedóttir, A.: A roadmap for producing wind turbine blade coating leading edge erosion atlases: Preliminary results, Tech. rep., IEA Wind Task 46: Erosion of wind turbine blades, https://iea-wind.org/wp-content/uploads/2025/03/IEA_Wind_Task_46_WP2.6-RoadmapErosionAtlases.pdf, accessed: 2025-03-26, 2025a.

Pryor, S. C., Coburn, J. J., and Barthelmie, R. J.: Spatiotemporal Variability in Wind Turbine Blade Leading Edge Erosion, Energies, 18, https://doi.org/10.3390/en18020425, 2025b.

Schalkwijk, J., Griffith, E. J., Post, F. H., and Jonker, H. J. J.: High-Performance Simulations of Turbulent Clouds on a Desktop PC: Exploiting the GPU, Bulletin of the American Meteorological Society, 93, 307–314, http://www.jstor.org/stable/26218643, 2012.

Shankar Verma, A., Jiang, Z., Ren, Z., Caboni, M., Verhoef, H., van der Mijle-Meijer, H., Castro, S. G., and Teuwen, J. J.: A probabilistic long-term framework for site-specific erosion analysis of wind turbine blades: A case study of 31 Dutch sites, Wind Energy, 24, 1315–1336, https://doi.org/10.1002/we.2634, 2021.

Slot, H.: A fatigue-based model for the droplet impingement erosion incubation period, Ph.D. thesis, University of Twente, Enschede, The Netherlands, ISBN: 978-90-365-5191-5, DOI: 10.3990/1.9789036551915, 2021.

Slot, H., Gelinck, E., Rentrop, C., and van der Heide, E.: Leading edge erosion of coated wind turbine blades: Review of coating life models, Renewable Energy, 80, 837–848, https://doi.org/10.1016/j.renene.2015.02.036, 2015.

Slot, H., Caboni, M., and van der Mijle Meijer, H.: Drop size effect on leading edge erosion incubation period and erosion rate – A review, in preparation, 2025.

Storey, R. and Rauffus, R.: Mesoscale-coupled Large Eddy Simulation for Wind Resource Assessment, Journal of Physics: Conference Series, 2767, 052 040, https://doi.org/10.1088/1742-6596/2767/5/052040, 2024.

Thurai, M., Schönhuber, M., Lammer, G., and Bringi, V.: Raindrop shapes and fall velocities in "turbulent times", Advances in Science and Research, 16, 95–101, https://doi.org/10.5194/asr-16-95-2019, 2019.

Tilg, A.-M., Vejen, F., Hasager, C. B., and Nielsen, M.: Rainfall Kinetic Energy in Denmark: Relationship with Drop Size, Wind Speed, and Rain Rate, Journal of Hydrometeorology, 21, 1621 – 1637, https://doi.org/10.1175/JHM-D-19-0251.1, 2020.

Verma, A. S., Jiang, Z., Caboni, M., Verhoef, H., van der Mijle Meijer, H., Castro, S. G., and Teuwen, J. J.: A probabilistic rainfall model to estimate the leading-edge lifetime of wind turbine blade coating system, Renewable Energy, 178, 1435–1455, https://doi.org/10.1016/j.renene.2021.06.122, 2021.

460 Vimalakanthan, K., van der Mijle Meijer, H., Bakhmet, I., and Schepers, G.: Computational fluid dynamics (CFD) modeling of actual eroded wind turbine blades, Wind Energy Science, 8, 41–69, https://doi.org/10.5194/wes-8-41-2023, 2023.

Wind Energy - The Facts: Tip Speed Trends, https://www.wind-energy-the-facts.org/tip-speed-trends.html, accessed: 2024-12-06, 2024.